



Master's Thesis submitted in fulfillment of the requirements for the degrees of
Master of Engineering
Master of Science

Thermal and structural finite element analysis of ECRH reflector tile of Wendelstein 7-X

Author:
Nicolas Olive-Leriche
Mechanical engineering/Applied physics and
physical engineering

Academic supervisor:
MdC. MATHIEU SOLAR
INSA Strasbourg
Institut Charles Sadron

Professional tutor:
MIKHAIL KHOKHLOV
Max Planck Institute for Plasma Physics

Acknowledgement

Merci beaucoup rpz67

*sincerely,
Nicolas*

Abstract

Résumé

Contents

1	INTRODUCTION	1
1.1	PROBLEM DEFINITION AND OBJECTIVES	1
1.2	STRUCTURE OF THE THESIS	2
2	THEORETICAL FRAMEWORK	3
2.1	GENERAL THEORY OF FUSION REACTORS	3
2.2	W7-X SYSTEMS	6
2.3	HEAT TRANSFER	7
2.3.1	General problem of heat exchange	7
2.3.2	Heat conduction	8
2.3.3	Convective heat transfer	8
2.3.4	Thermal radiation	9
2.4	SOLID MECHANICS	9
2.5	FINITE ELEMENT METHOD	9
3	STATE OF THE ART	10
3.1	THE ECRH TZM REFLECTOR TILE ASSEMBLY	10
3.2	PREVIOUS ANALYSES OF THE ECRH REFLECTOR TILE	12
3.3	ISSUES OF THE MODEL	14
4	METHODS AND CONFIGURATIONS	15
4.1	MATERIAL PROPERTIES AND PHYSICAL MODELS	15
4.1.1	Thermal properties	16
4.1.2	Mechanical properties	16
4.2	CONTACT CONFIGURATION	20
4.2.1	Initial contact setup	20
4.2.2	Field coupling and contact configuration	22
4.3	PLASMA HEAT LOAD	23
4.4	MODELLING OF THE ECRH BEAM	24
4.4.1	Calculation of the integration coefficients	24
4.4.2	Coding strategy and implementation in ANSYS®	28
5	ANALYSES SETUP AND RESULTS	31
5.1	STEADY-STATE THERMAL ANALYSIS	31
5.1.1	Calculation of the surface integrals	31
5.1.2	Comparison between old and new TZM tile design	35
5.1.3	Film coefficient influence on thermal behavior	37
5.1.4	Load case influence on thermal behavior	38
5.2	TRANSIENT THERMAL ANALYSIS	39
5.2.1	Analysis for HE1 to HE4 pulse duration	39
5.2.2	Analysis for HE1 pulse length and cooldown	41
5.3	STATIC STRUCTURAL ANALYSIS	42
5.3.1	Analysis of the boundary conditions influence	42
5.3.2	Contact status after calculations with 100 % contact between TZM-tile and Sigraflex thermal gasket	45
5.4	COUPLED FIELDS ANALYSIS	46
5.4.1	Introduction to coupled fields analysis	47
5.4.2	Static thermal-structural analysis of the tile assembly	48
6	CONCLUSION AND RECOMMENDATIONS	50

List of Figures

2.1	<i>Nuclear binding energy vs. mass number.</i>	3
2.2	<i>Fusion cross sections for various fusion reactions (D-T, D-He³ and D-D) versus ion temperature. [5]</i>	4
2.3	<i>Velocity averaged cross section $\langle \sigma v \rangle$ for various fusion reactions (D-T, D-He³ and D-D) versus ion temperature. [5]</i>	4
2.4	<i>Schematics of a Tokamak confinement, courtesy of C. Brandt</i>	5
2.5	<i>Schematics of a Stellarator confinement, courtesy of C. Brandt</i>	6
3.1	<i>Different views of the ECRH launchers and reflector tiling</i>	10
3.2	<i>Components and montage of the reflector tile assembly</i>	11
3.3	<i>Physical constraints for burning plasma PFCs [7]</i>	12
3.4	<i>FE model of the tile assembly [4]</i>	12
3.5	<i>Model of the tile assembly [10]</i>	13
3.6	<i>Temperature field (in °C) of the CuCrZr heat sink for the two heat fluxes [10]</i>	14
4.1	<i>Material assignation</i>	15
4.2	<i>Contact configuration for thermal and structural analysis</i>	21
4.3	<i>Contact status comparison</i>	21
4.4	<i>Modules of the heat shield (HS)</i>	23
4.5	<i>Representation of the two ECRH beam heat flux distribution cases</i>	24
4.6	<i>3D graph of the Heaviside step function defined over Ω</i>	27
4.7	<i>Heat flux distribution script for APDL</i>	29
5.1	<i>3D model of the TZM tiles for integral calculation</i>	31
5.2	<i>Model of the 1-D conduction test</i>	32
5.3	<i>Prescribed temperature of the ANSYS® model for surface integral calculations</i>	33
5.4	<i>Prescribed temperature of the ANSYS® model for surface integral calculations</i>	35
5.5	<i>Temperature fields for resp. old and new design. View A is the entire model, view B is just the TZM reflector tile and view C is the CuCrZr heat sink.</i>	36
5.6	<i>Maximum part temperature in function of load case. The maximum operational temperature is not fixed for CuCrZr.</i>	37
5.7	<i>Maximum heat sink temperature for two film coefficients. View A is the old TZM reflector tile design's heat sink and view B is the new TZM reflector tile design's heat sink</i>	38
5.8	<i>Maximum heat sink temperature in function of load case. View A is for plasma heat load ONLY case, View B is for plasma heat load + ECRH axisymmetric heat load, View C is for plasma heat load + ECRH NON-axisymmetric heat load and View D is for plasma heat load + ECRH axisymmetric heat load with J. Zhu parameters.</i>	38
5.9	<i>Table of the pulse durations [8]</i>	39
5.10	<i>Evolution of the temperature ratio $\frac{\theta_{\max}^{\text{part}}}{\theta_0}$ in function of time (with echelon at all HE pulse steps). Calculation done for the load case : Plasma heat load + ECRH axisymmetric heat load.</i>	40
5.11	<i>Evolution of the maximum temperature of the CuCrZr heat sink for 100 s pulse and 300 s cooldown.</i>	41
5.12	<i>Boundary conditions for the reference case (0).</i>	42
5.13	<i>View of the third of module H – 02 with the support parts and heat sinks of adjacent tiles. A is the support that will be jointed and B is the fixed support</i>	43
5.14	<i>Maximum displacement of the module in function of freed DoF.</i>	44
5.15	<i>Contact area reduction phenomenom.</i>	45
5.16	<i>Manual coupling method.</i>	45
5.17	<i>Temperature in °C. Application of the manual coupling.</i>	46

5.18 Contact shrinking after structural recalculation.	46
5.19 Fields coupling.	47
5.20 Coupled analysis of CuCrZr heat sink per load case. A is plasma heat load only, B is plasma heat load + ECRH axisymmetric heat load, C is plasma heat load + ECRH non-axisymmetric heat load, D is plasma heat load + ECRH axisymmetric heat load (J. Zhu parameters) [10].	48

Acronyms

BCs Boundary Conditions. 2, 42

BM Baffle Module. 12

CuCrZr Copper Nickel Zirconium. vi, vii, 11, 13, 14, 15, 16, 17, 20, 22, 35, 36, 37, 41, 45, 48, 49

DoF Degrees of Freedom. vi, 43, 44, 48

ECRH Electron Cyclotron Resonance Heating. v, vi, 2, 7, 10, 11, 12, 13, 15, 20, 23, 24, 26, 28, 30, 31, 33, 34, 35, 37, 40, 41, 49

ELMs Edge Localized Modes. 11

FE Finite Element. 11, 35, 42, 45

HS Heat Shield. vi, 7, 23

KiP Komponenten im Plasmagefaß. 11

NBI Neutral Beam Injection. 11, 16, 41

OP1 Operation Phase 1. 1, 12

OP2 Operation Phase 2. 1, 2, 11, 12, 14, 15, 39

PFCs Plasma Facing Components. vi, 1, 5, 11, 12, 23

PV Plasma Vessel. 35, 42, 43

Sigraflex Sigraflex. 11, 15, 16, 19, 20, 22

SS Stainless Steel. 14, 15, 16, 18, 20, 35, 42

TZM Titanium Zirconium Molybdenum. v, vi, 10, 11, 12, 15, 16, 17, 20, 31, 32, 33, 35, 36, 37, 38, 43, 45, 46

W7-X Wendelstein 7-X. 1, 11, 39

1 | INTRODUCTION

NUCLEAR fusion has been the subject of many years of research and different experiments conducted at all scales. This craze is mainly due to the possibility of clean, renewable and safe nuclear power generation. This idea of generating electricity via the fusion of light atomic nuclei finds its roots in the early 1950s when physicists tried different ways of containing a plasma using different techniques, one of which is called magnetic confinement. To know why such devices are necessary, a look at the physics behind nuclear fusion could help. Fusing light atomic nuclei require them to come close enough for the strong nuclear force to overcome the electrostatic force pushing them apart. One way to approach one nucleus to the other close enough to surpass the so-called Coulomb barrier is to heat the atoms to high temperatures or accelerate those particles enough to attain such energies. At those energies, the fuel becomes a hot plasma and can no longer be contained in a classical confinement.

Plasma is the fourth state of matter, consisting of ionized gas where atoms lose electrons. This ionization results in a mixture of positively charged ions and free electrons, making plasma distinct from solids, liquids, and gases. Plasmas exhibit unique properties, including responsiveness to magnetic fields and the ability to conduct electricity. They are prevalent in phenomena like stars, lightning, and certain man-made technologies such as fluorescent lights and plasma TVs. The pursuit of effective confinement for fusion plasma introduces various challenges of a complex nature. Stability concerns arise from inherent plasma instabilities, contributing to disruptions and energy dissipation. The prudent management of heat generated by fusion reactions assumes paramount importance to mitigate potential damage to plasma facing components. The research for materials suitable for the plasma facing components with enhanced durability requires overcoming challenges associated with extreme conditions, including elevated temperatures, neutron bombardment, and erosion.

Magnetic confinement, a crucial aspect of fusion devices, necessitates intricate manipulation of magnetic fields to attain stability and sustain plasma confinement. Establishing an energy equilibrium, where input aligns with output, constitutes a foundational imperative for realizing ignition in fusion reactions. The control of turbulence and transport phenomena within the plasma is essential to preclude unwarranted particle and energy transport, optimizing overall performance. The delicate equilibrium governing plasma density and temperature, vital for sustained fusion reactions, necessitates meticulous control and stability. Addressing these intricacies assumes pivotal significance in advancing fusion research and realizing the potential of fusion energy as a scientifically viable and sustainable power source. Wendelstein 7-X (**W7-X**) is an experimental Stellarator fusion device located at the Max Planck Institute for Plasma Physics (IPP) in Greifswald, Germany. The purpose of **W7-X** is to investigate the feasibility of generating energy through nuclear fusion.

1.1 PROBLEM DEFINITION AND OBJECTIVES

W7-X enters its enhanced operation phase called **OP2**. This operation phase aims to improve confinement time and heating power. To achieve longer runs and attain steady state operation, many different plasma parameters such as the temperature, the density and the pressure need to be fully controlled and piloted precisely. To gain this control and understand more the complex plasma dynamics of the reactors, longer plasma discharges will take place and provide to the physicists the desired data. Because the plasma discharges are longer and the plasma heated at higher powers than in Operation Phase 1 **OP1**, the components surrounding the plasma, especially the plasma facing components (**PFCs**) will be exposed to higher heat flux for a longer period of time. This will lead to increased wear on the system components due to high heat fluxes and can lead to mechanical failure. To assess this risk of failure, the engineering analysis group of the Experimental Plasma Physics 5 department conducts many different numerical analysis campaigns to predict the behavior of the device under special load cases.

In order to set boundaries on the pulses of **OP2** and validate the proper functioning of the various subsystems, the thermal analyses as well as the mechanical analyses of various in-vessel components both steady and unsteady is carried out by the engineers. After early calculations, it was shown that. It is necessary for the **ECRH TZM**-reflector tile to accommodate for high steady state heat flux. Steady state is assumed for the analysis since the plasma impulse is considered of long duration and the thermal equilibrium of the reflector tile attained. It is crucial to properly design and dimension the tile in order to allow the new operational parameters. Based on the modified TZM-reflector tile, thermal and structural finite element analyses of different load cases and boundary conditions **BCs** will be conducted to validate the new design. Following the results of these analyses, the engineers will be able to set operational boundaries if necessary or validate the design and proceed with the operation. The results will also allow to know the different maximum operational parameters such as maximum operation time. The reliability of the calculations will influence the decision made and thus needs to be estimated to avoid any significant error between the FE model and the real life behavior.

First, a literature research is carried out to understand the physics involved in those phenomenon such as the link between temperature and mechanical properties of materials or the physics of radiative heat transfer. The reading of documents assessing those issues also helps put into context this work and lie the basis upon which this Thesis is being lead. Because this is entirely simulation based, the proper functioning of the analyzed components will be proved by locating their performances within an operational space defined by the designers under various load cases and meshes. In addition to that, this work is separated into main tasks, the steady state as well as transient thermal and mechanical FEA of the **ECRH TZM**-reflector tile. To do that, the modelling and setup of the different geometries as well as the clarification and characterization of the physics, material properties and **BCs** and the analyses and discussions about the results will be necessary.

1.2 STRUCTURE OF THE THESIS

In the first third section of the Thesis, the theoretical foundations for practical work are explained. These include the basics of nuclear fusion and fusion devices but also concepts of heat transfer and solid mechanics. This will help setting up a link between the two and allow building and propose a performance indicator based on positions in an operational space to validate proper functioning.

The second and the third sections, the methods and models as well as the results and the discussions of the analyses will be done and concluded at the very end of this work.

2 | THEORETICAL FRAMEWORK

In this chapter, the basics of fusion such as nuclear physics and magnetic confinement are explained. In addition to that, the construction and the different systems of the W7-X are also explained to give an overview on the device and its auxiliary components. Heat transfer theory as well as solid mechanics including plasticity and fatigue constitute the basis of the work and the complex equations of these theories solved using Finite Element Analysis. These theories are necessary for the completion of this work and are therefore reminded in this chapter.

2.1 GENERAL THEORY OF FUSION REACTORS

The principle of a nuclear fusion power plant is to make the energy released by the fusion of light atomic nuclei usable. Nuclear fusion which represent the fusing of atomic nuclei together is only achievable if they come close enough to surpass the electrostatic repulsion forces and have the strong nuclear force fuse the nucleons together. Due to electrostatic repulsion forces also called Coulomb barrier, the nuclei repulse each other thus preventing the reaching of the necessary distance (because the strong nuclear force has a very limited range, 10^{-15} m) [2][5] for fusion. Furthermore, the repulsion forces increase with the number of protons in the nucleus or its size. The energy required to fuse two nuclei become subsequently greater.

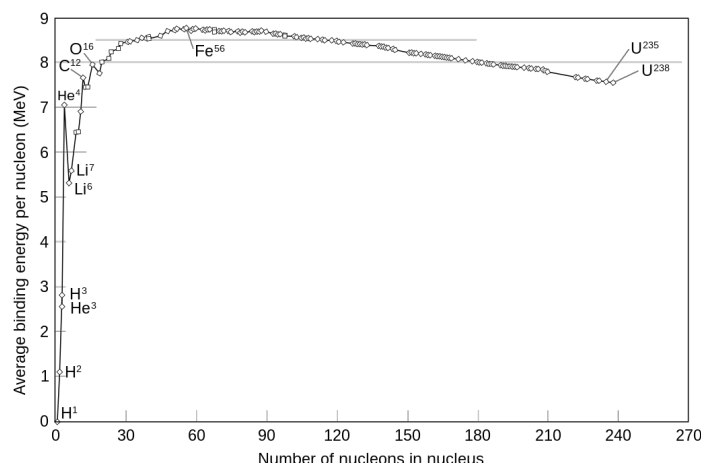


Figure 2.1: Nuclear binding energy vs. mass number.

The different nuclear reactions for transforming hydrogen into helium are [2]:



or



On Figure 2.2, the cross section for various reactions are graphed in function of the ion temperature. The cross section represents the area on which it is possible for nuclei to collide and subsequently fuse together. The higher the cross section, the higher the nuclei are likely to collide with each other. For lower ion temperatures, the Deuterium-Tritium reaction has the biggest cross section. The easiest way to initiate fusion is by the Deuterium–Tritium reaction, which releases 17.6MeV , 14.1MeV in the neutron and 3.5MeV in the alpha particle. [5]

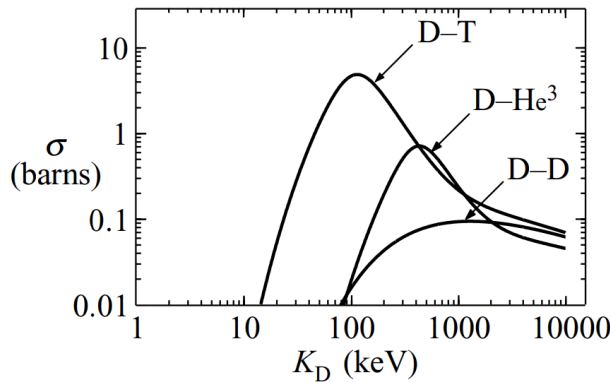


Figure 2.2: Fusion cross sections for various fusion reactions (D-T, D-He³ and D-D) versus ion temperature. [5]

When the cross section is known, is it possible to calculate the reaction rate for the main fusion reactions. The reaction rate is noted $\langle \sigma v \rangle$. These results are illustrated in Figure 2.3 as curves of $\langle \sigma v \rangle$ vs. ion temperature T . It is possible to observe that the peak value of the reation rate is $9 \times 10^{-22} \text{m}^3 \text{s}^{-1}$ at 70keV for the D-T fuel mix.

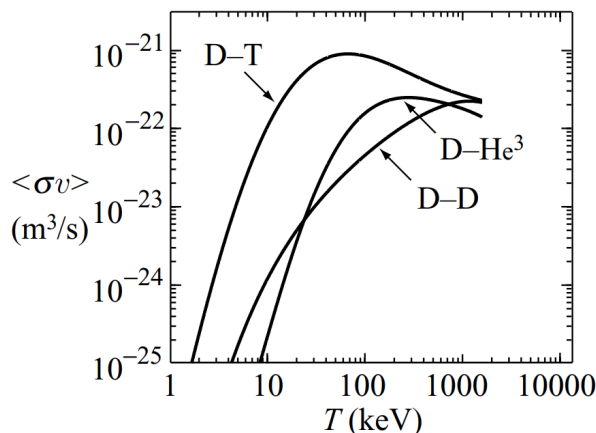


Figure 2.3: Velocity averaged cross section $\langle \sigma v \rangle$ for various fusion reactions (D-T, D-He³ and D-D) versus ion temperature. [5]

As said previously, the energies to achieve nuclear fusion are important. One solution to this problem is to give the correct amount of kinetic energy to the nuclei in order for them to overcome the Coulomb barrier. This kinetic energy is measured in Electron-Volts and is obtained by heating the fuel to high temperatures. The temperature thus reaches 100M to 200M°C [2], which is hotter than the sun's core. At those temperatures, the fuel becomes a plasma, which is often considered as the fourth state of matter. Plasma is also called the highest state of aggregation of a substance designated. In this aggregate state, the internal energy is far higher than the binding energy between the electrons and the nuclei. This means that the electrons can move freely. Plasma differs greatly in its properties from normal gases.

The important temperature of the plasma forces various measures to be taken to ensure that the Materials built into the fusion reactor near the plasma provide maintained thermal insulation and compensate for the resulting expansion pressure. A solution to this problem is the exploiting of the Lorenz force affecting the charged particles of the plasma. The idea is, at least for magnetic confinement, to trap the plasma inside a magnetic cage. This will help levitating the plasma and control its shape and position to avoid touching any PFCs. The distance between the plasma and the PFCs is crucial since contact could generate plasma turbulence or contaminate the plasma with impurities, reducing the quality of it. Different systems where developed to build such a confinement.

There are two different type of magnetic confinement concepts that are widely know and developed, the Tokamak and the Stellarator. These two magnetic confinement devices are both based on a toroidal geometry, the difference between the two of them being the way the plasma is confined. In a Tokamak machine, the plasma is confined using planar toroidal magnetic coils. Those coils help create the toroidal magnetic field component of the confinement. Although this seems like a good confinement, other problems still need to be addresses such as the effect of particle drift. This drift is due to pressure gradients and inhomogeneities in the magnetic field inside the plasma and leads to a drift of the particles towards the outer diameter of the Tokamak. This complex particle transport phenomenon can be mitigated by introducing a poloidal component to the magnetic field, causing a rotation of the plasma around its toroidal axis. To achieve this magnetic field, Tokamaks use a solenoid coil placed at the center of the torus. This solenoid coil acts as a primary transformer coil, a time-varying electric current generate a varying magnetic field which itself induce an electric current inside the plasma. The resulting movement of charges inside the plasma generate a poloidal magnetic field, the plasma is then generating its own magnetic field. This electric current can also be used to heat up the plasma, it is called ohmic heating.

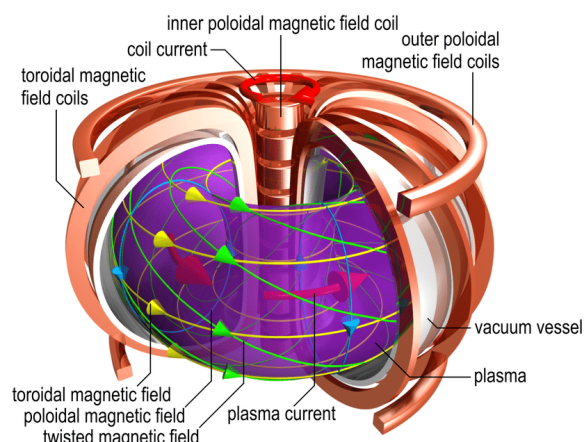


Figure 2.4: Schematics of a Tokamak confinement, courtesy of C. Brandt

While this solution is good, there are problems with it. The main issue is the inherently transient process. The poloidal component of the magnetic field can only be generated as long as the current in the solenoid coil varies. This means that the reactor can only run in pulses and steady-state isn't currently achievable.

Another solution for generating the poloidal magnetic field is to twirl the plasma in such a shape, that the drift phenomenon disappears. This solution is the Stellarator. The Stellarator was first introduced by Lyman Spitzer in the 1950s. This technology was put aside because of technical difficulties and because the Tokamaks presented better performances. The Stellarators use a complex set of magnets allowing to generate a precise magnetic field allowing the plasma to not experience significant drift. Contrary to Tokamaks, Stellarators plasmas don't have a plasma current. This solution also helps with confinement, as the magnetic field can be adjusted to accommodate for the strict equilibrium conditions. The absence of plasma current also means that Stellarators can be operated in steady-state since no current induction is needed, thus being more suitable for power plants. Although allowing improved plasma confinement, Stellarators are plagued by complex geometries that are often too complex to be feasible.

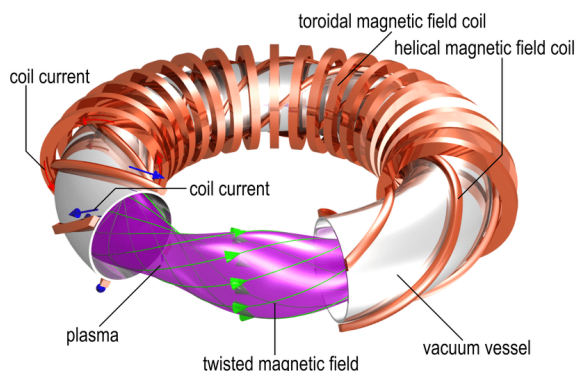


Figure 2.5: Schematics of a Stellarator confinement, courtesy of C. Brandt

The goal of those magnetic confinement fusion reactors concepts is to propose a new way of producing atomic energy while avoiding the drawbacks of traditional fission reactors (ie. Management of radiation, production of highly radioactive long half-life elements, limited fuel supply...). Although fusion energy is attractive, many problems still need to be addressed such as tritium breeding issues or neutron transport and interaction with the structure.

2.2 W7-X SYSTEMS

The Wendelstein 7-X (W7-X) is a stellarator nuclear fusion experiment with a significant history that underscores its importance in fusion research. The idea for W7-X was born in the late 1980s and early 1990s, aimed at testing the viability of stellarator design for sustained fusion reactions. This built upon the success of its predecessor, Wendelstein 7-AS.

In 1996, the German government approved the construction of W7-X, with substantial funding from the European Union and international partners. Construction began in 1997 at the Max Planck Institute for Plasma Physics (IPP) in Greifswald, Germany. This phase involved assembling complex superconducting magnetic coils and a highly precise vacuum vessel, presenting numerous technical challenges that required innovative solutions.

By 2014, the assembly of W7-X was completed, marking a major milestone. The machine produced its first plasma on December 10, 2015, demonstrating the functionality of its design and construction. Following this achievement, W7-X entered its experimental phase. Initial experiments focused on achieving and maintaining stable plasma conditions, testing heating methods, and studying plasma behavior.

Over the subsequent years, W7-X achieved several key milestones, including sustained plasma discharges lasting up to 100 seconds and significant advancements in plasma heating and density. These experiments provided valuable insights into plasma confinement and stability, moving closer to the goal of long-pulse operations lasting up to 30 minutes. This capability is critical for the development of future fusion power plants, as it demonstrates the potential of stellarators for continuous operation.

Research continues to optimize plasma performance, improve heating and control techniques, and deepen the understanding of stellarator physics. The Wendelstein 7-X remains a cornerstone of global fusion research, contributing valuable data and insights that support the broader goal of developing practical and sustainable fusion energy.

2.3 HEAT TRANSFER

In this section, the fundamental principles and governing equations and each heat transfer mode are explored. The TZM-reflector tile is a highly constrained mechanical part that of the **HS**. This part will be exposed to plasma radiation as well as the **ECRH** beam. The heat transfer in this system is complex and need a good understanding of the theory to model it as good as possible.

The heat loads on the **ECRH** reflector tile are specified further in the thesis but the theory first needs to be explained, at least what will be needed for this task.

2.3.1 General problem of heat exchange

Heat exchange happens all the time and everywhere in nature, from the sun's radiative power to the heat transfer on the surface of the skin. Historically, heat was considered as some sort of *flow* that would flow from one hot object to another colder object [6]. The idea of an invisible fluid flowing from a body to another called *Caloric* was first considered to explain this heat transport. While the caloric theory of heat exchange is acceptable to consider such a concept for explaining heat transport, there are more modern approaches to heat exchange that will be discussed later [6]. The general problem of heat transfer involves understanding how thermal energy is transported from one place to another. The modern approach to heat transfer is the *kinetic* theory. Heat is defined to be the average Velocity of the particles within a system. This approach helps to understand what heat is physically [1]. Heat exchange can be seen in many different situations and takes place in every medium and different modes. Leaving a hot house during winter with a door open and having the hot air making its way out, hummingbirds using a counterflow heat exchanger in their feet to regulate their body temperatures [9] or inadvertently touching a hot pan are all examples of heat exchange between mediums and objects [6]. It respects some rules such as the flow direction, from hot to cold.

Not only in nature but also in industry, heat is heavily used for/or is a product of chemical processes. Steam boilers convert chemical energy into heat to generate steam and then generate electricity, this is also true for nuclear power plants, using the heat generated by fission reactions to generate steam. Heat is generated in combustion engines and needs to be evacuated meanwhile in fridges, heat is pumped to decrease the temperature in a chamber. Those devices all use some sort of heat transfer in order to work properly. Heat exchange is also present throughout of fusion devices at many different levels such as inside the plasma as well as the first wall components and the pumping system. Correctly modelling heat exchange as well as understanding the physical phenomena behind the transfer of heat in thermal ma-

chines.

Thermodynamics is a theory about the dynamics and conversion of different energy forms heavily developed during the 19th century. It provides a very good framework in which it is possible to built a theory of heat exchange [6]. It is possible to derive the equation of heat transfer from the laws of thermodynamics. The first law of thermodynamics for a closed system, as taught in engineering programs, takes the following form:

2.3.2 Heat conduction

Conduction is the transfer of energy from the more energetic particles of a substance to the adjacent less energetic ones as a result of interactions between the particles [1]. Conduction can take place in solids, liquids, or gases. In fluids, conduction is due to the collision and diffusion of the molecules during their random motion. In solids, conduction is due to the combination of vibration of the molecules in a lattice and the energy transport by free electrons.

Lets consider steady-state heat conduction through a plane wall of thickness $L = \Delta x$ and area A . The difference of temperature or *gradient* is measured and is written $\Delta T = T_2 - T_1$. Experience has shown that the rate of heat transfer \dot{Q}_{cond} through the wall would double when the temperature gradient across the wall *or* when when the area A normal to the direction of heat transfer doubles. The rate of heat transfer would be halved when the thickness L doubled. Qualitatively, it is possible to conclude that the rate of heat conduction through a plane wall is proportional to the temperature gradient across the layers and the heat transfer area, but is inversely proportional to the thickness of the layer. The relation between the quantities is:

$$(Rate\ of\ heat\ conduction) \propto \frac{(Area)(Temperature\ gradient)}{Thickness} \quad (2.6)$$

Analytically, the mathematical law describing the conduction of heat is **Fourier's law of heat conduction**. The coefficient k is the thermal conductivity, which is the ability of a certain material to conduct heat. It is possible to write this law using quantities and the equation is :

$$\dot{Q}_{cond} = -kA \frac{T_2 - T_1}{\Delta x} = -kA \frac{\Delta T}{\Delta x} \quad [W] \quad (2.7)$$

When $\Delta x \rightarrow 0$, the one-dimensionnal differential form of the equation is written:

$$\dot{Q}_{cond} = -kA \frac{dT}{dx} \quad [W] \quad (2.8)$$

On the left hand side of the heat conduction equation 2.8 \dot{Q}_{cond} describes the time derivative or temporal rate of change of the heat flux flowing though a surface. On the right hand side of the equation, k is the thermal conductivity. Usually, the thermal conductivity is a function of the temperature itself making this differential equation nonlinear.

2.3.3 Convective heat transfer

It was mentionned earlier that there are three basic mechanisms of heat transfer: conduction, convection, and radiation. Conduction and convection are similar in that both mechanisms require the presence of a material medium. But they are different in that convection requires the presence of fluid motion. Heat transfer through a solid is always by conduction, since the molecules of a solid remain at relatively fixed positions. Heat transfer through a liquid or gas, however, can be by conduction or convection, depending on the presence of any bulk fluid motion. Heat transfer through a fluid is by convection in the presence of bulk fluid motion

and by conduction in the absence of it.

2.3.4 Thermal radiation

2.4 SOLID MECHANICS

2.5 FINITE ELEMENT METHOD

3 | STATE OF THE ART

In this chapter, the design, the use and the architecture of the reflector tile will be explained. Moreover, the already existing analyses and results will be discussed to give context and insight about the situation and the functioning of this system.

3.1 THE ECRH TZM REFLECTOR TILE ASSEMBLY

The reflector tile is used to reflect the **ECRH** beam back into the plasma to limit energy loss. This reflector tile is placed in a particular position inside of the stellarator.

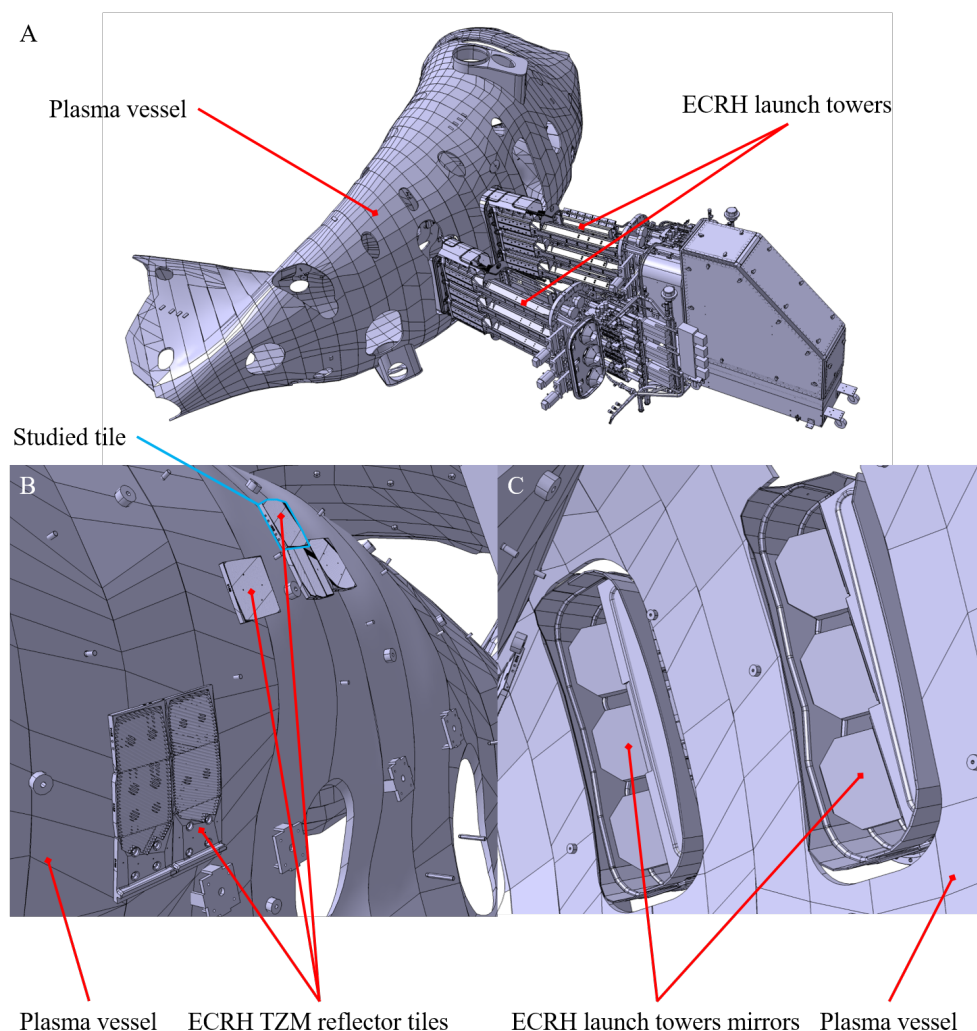


Figure 3.1: *Different views of the ECRH launchers and reflector tiling*

The different views from figure 3.1 are:

- A: View of the plasma vessel and the two ECRH launchers
- B: View of the ECRH TZM reflector tiles
- C: View of the launcher mirrors

The reflector tiles face the plasma and are a component of the PFCs and are placed in front of the ECRH launch towers. A reflective alloy made of titanium zirconium and molybdenum abbreviated TZM was chosen to build the reflector tile. The reflector tile is mounted on a copper chromium zirconium heat sink that is brazed onto a stainless steel cooling pipe. The ECRH reflector tile is placed on one of the modules composing the in-vessel components or KiP.

The reflector tile has a simple assembly. The TZM reflector tile is held in place using holding pins screwed on the side of the tile. The holding pins hold the head of the bolt back. A nut is screwed on the bolt and using a 270° turn, the nut pushes again a stack of three INCONEL Belleville washers. The washers, acting like a preloaded spring, push against the CuCrZr heat sink, applying a force on the Sigraflex thermal gasket which thermally separates the TZM tile and the CuCrZr heat sink.

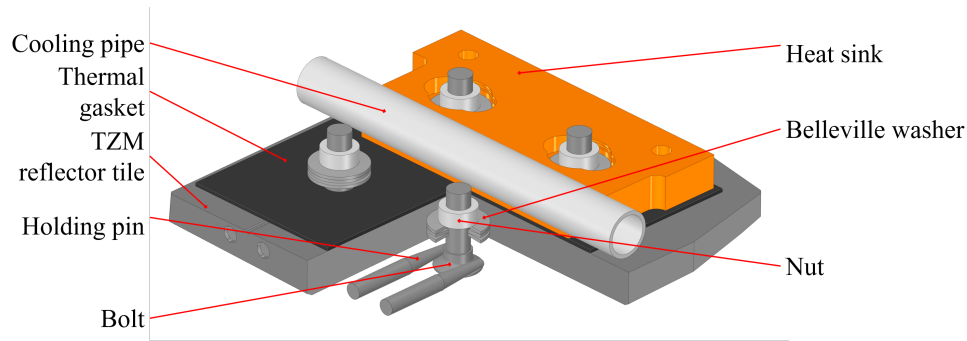


Figure 3.2: Components and montage of the reflector tile assembly

The reflector tile will be exposed to high heat fluxes that can be decomposed into two different sources (those two different heat sources will be implemented in the FE model for the analysis):

- Plasma heat load (*radiative and convective heat loads*)
- ECRH heat load

In a real powerplant condition (using Deuterium-Tritium mix as fuel), the PFCs would be exposed to other physical constraints and scenarios, in particular the neutron flux generated by the fusion reaction (generating defects and transmutations in the materials) or the diffusion of hydrogen into the material of the first walls potentially negatively affecting the mechanical properties and behavior of the first wall component materials. Highly dynamic phenomena such as Edge Localized Modes (ELMs) or disruptions can also be challenging for the first walls.

In the case of W7-X, in particular for OP2, no neutrons will be produced nor the heat fluxes reach powerplant-like values. It is still important to keep these considerations in mind to design the most effective PFCs and prepare for burning plasma, especially for reflector tiling or NBI dump tiling.

Those constraints can be summarized:

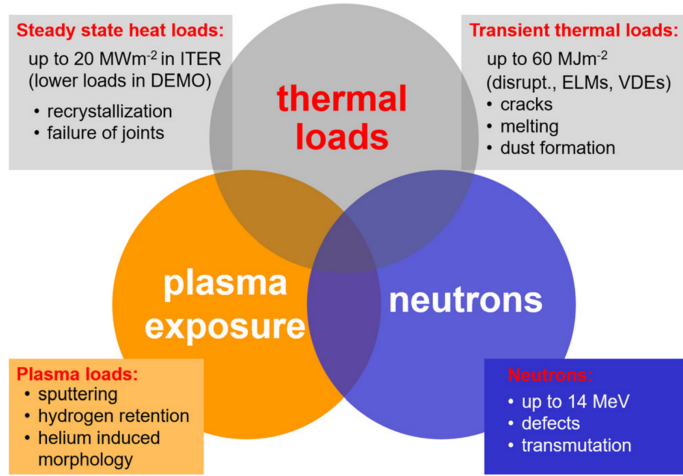


Figure 3.3: Physical constraints for burning plasma PFCs [7]

3.2 PREVIOUS ANALYSES OF THE ECRH REFLECTOR TILE

In order to reflect the ECRH beam into plasma back, some TZM tiles were suggested to substitute the BM graphite tiles in specific positions. The idea was to limit power loss due to absorption of the ECRH beam by the graphite tiles. After OP1.2 it was decided to increase the size of the TZM tile. Due to the fact the tile has been never analyzed in details, corresponding thermal and structural analysis is to be performed to assess the performance of the tile in OP2.

For OP2, plasma discharge duration will be increased thus exposing the PFCs to longer heat loads. The “worst” tile had been selected during discussion between Victor Bykov and Torsten Stange and was analyzed. Those analyses aimed to give insight about the thermal and structural integrity of the ECRH reflector tile during the plasma discharges with OP2 specifications.

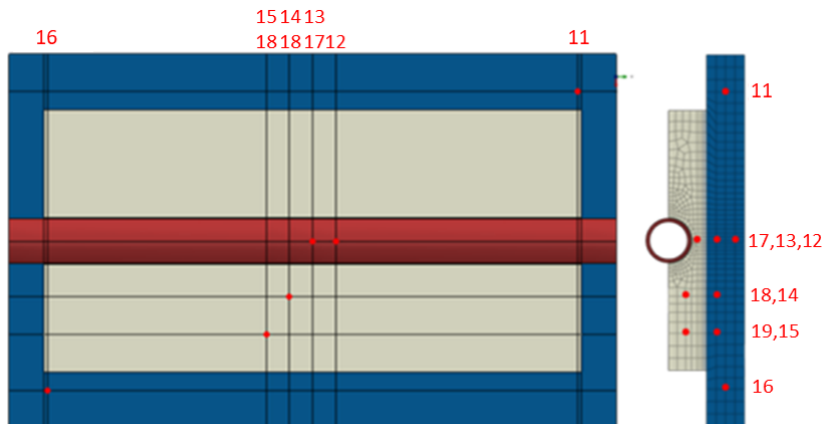


Figure 3.4: FE model of the tile assembly [4]

Different analyses such as transient thermal and fatigue analyses were performed by

various engineers to assure proper functioning of the tile. One of those analyses were performed by Joris Fellinger in 2013 and was the thermal-mechanical assessment of heat shields and baffles [4]. The analyses were performed on a simplified model *see figure 3.4* of the tile and calculated using Dassault Systèmes Abaqus. Perfect thermal contact between the parts was also assumed to simplify the model. The heat pulse was simplified to be a step signal lasting for about 90 s. Models for fatigue dimensioning and material properties were defined and used in this work. Thermal properties of the different materials used are also given and important for the rest of the work.

The effect of the boundary conditions, in particular restraining the axial displacement of the steel cooling pipe has a non-negligible and detrimental influence on the plastic strain [4]. This conclusion is going to be seen later in this work regarding the structural analysis.

In this work, a discussion about the thermal performances of the brazing between the heat sink and the cooling pipe or the Sigraflex thermal gasket also stated that these moderately affected the heat transfer within the tile assembly. On the other hand, the annealing of alloys and the temperature-dependant mechanical properties are a concern and the issue of having uncertain annealing of the CuCrZr due to thermal activation arose [4]. This will be an issue discussed later in the topic of this work.

Later, Jiawu Zhu was tasked to analyse the behavior of the tile and performed a complete thermo-mechanical analysis of the tile assembly. The model used by J. Zhu was quite different from the model of J. Fellinger because it featured the actual geometry of the reflector tile. The whole reflector tile as well as the thermal gasket, heat sink and cooling pipe were implemented in the model. the bolting system also included a simplified version of the Belleville washers and the bolts didn't have the same geometry.

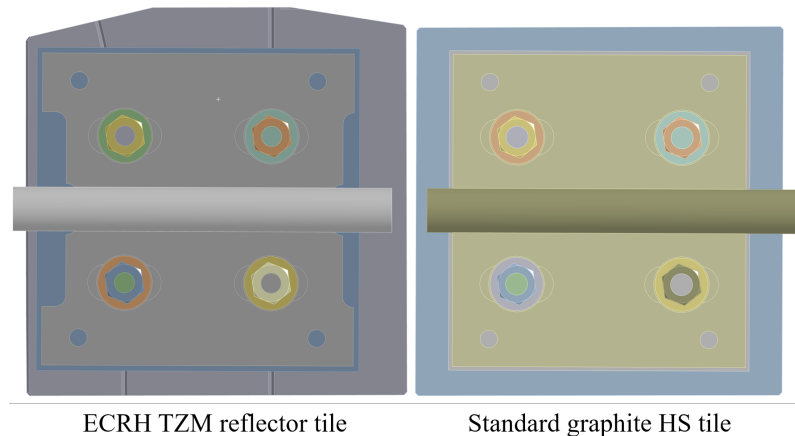


Figure 3.5: Model of the tile assembly [10]

The analyses carried out by J. Zhu included another graphite tile of the heat shield to compare the results. The results were divided into two categories:

- Thermal analysis
- Structural analysis (ie. fatigue analysis)

For the thermal analysis, the plasma heat load was initially 250kWm^{-2} and the ECRH heat flow was 912W over a gaussian distribution to model the beam stray radiation. The results showed overheating of the CuCrZr heat sink (in steady-state operation) and the plasma heat load was subsequently lowered to avoid reaching critical temperature of the bronze alloy of

the heat sink. The heat flux was lowered to 220 kW m^{-2} which represents 88% of the specified heat load for OP2 (which is not enough to respect the operational specifications of OP2). The thermal analysis was redone (see 3.6) with the new heat load and showed acceptable temperature field for the heat sink. The issue with the recrystallization (as stated in [4]) of the CuCrZr still is relevant for these analysis.

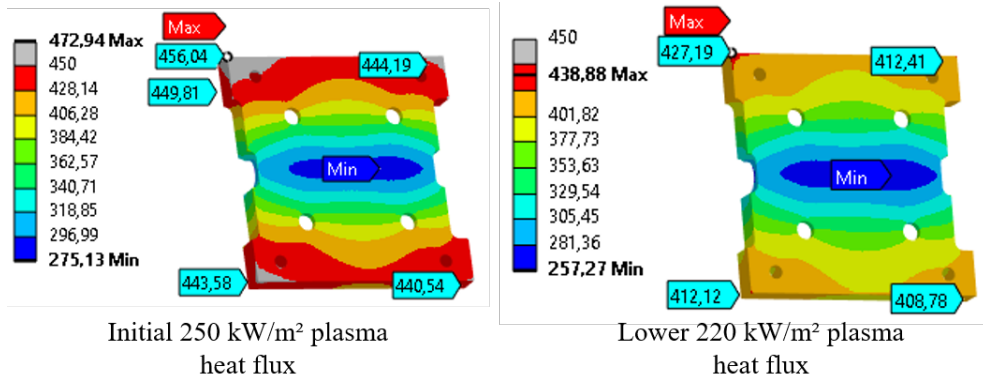


Figure 3.6: Temperature field (in $^{\circ}\text{C}$) of the CuCrZr heat sink for the two heat fluxes [10]

The structural analysis of the tile assembly was done by importing the temperature field in the mechanical analysis. one end of the cooling pipe is fixed and the other one let loose. The bending of the whole assembly is thus not constrained. The main point of concern was the assumption of perfect brazing between CuCrZr heat sink and the SS cooling pipe. In reality, it is possible that cracks may exist in the braze connection which could end up initiating a crack damaging the brazed connection [10]. While fracture mechanics are known, establishing a framework to effectively model multi-material interface fracture expansion remains a challenge that is out of the frame for this task.

3.3 ISSUES OF THE MODEL

After the analyses done by J. Fellinger and J. Zhu, different issues were shown. The first issue is one of the parameter for the cooling pipe. The value of the film coefficient for the cooling pipe convection used by J. Zhu in his study [10] was set to be $30\text{ kW m}^{-2}\text{ °C}^{-1}$. This value is unlikely to be realistic and was discussed to reach at most $18\text{ kW m}^{-2}\text{ °C}^{-1}$ with a minimum value of $15\text{ kW m}^{-2}\text{ °C}^{-1}$. This gives the range of $3\text{ kW m}^{-2}\text{ °C}^{-1}$. The reduction of the film coefficient could prevent optimal cooling and heat evacuation and needs to be assessed.

The recrystallization of the CuCrZr alloy could also negatively impact the mechanical properties. This phenomena is still not well known in this case because of lack of material data. The structural and fatigue behavior are also to be redone for 250 kW m^{-2} . The material properties also need to be revised to taken into account new material properties.

With that in mind, it is possible to build a new numerical model based on revised boundary conditions and material properties.

4 | METHODS AND CONFIGURATIONS

As stated in the state of the art; the object of these analyses is the **ECRH** TZM-reflector tile (ref. E821). To study the thermal and mechanical behavior of this in-vessel component, finite element analysis using the ANSYS® software will be carried out to evaluate the new design's performances and the proposed solution to the overheating of the CuCrZr heat sink issue. Coupled physics analyses, in particular one-way coupling and full coupling of thermal and structural analyses, will be used to assess the effects of the design changes and validate the proper functioning of the reflector tile in **OP2** design loads.

4.1 MATERIAL PROPERTIES AND PHYSICAL MODELS

One of the crucial point of this task are the material properties such as the thermal and mechanical properties and behavior. Those properties can have a big influence on the results of the calculations and they need to be carefully set to accurately model the real life metarial. As is in real life, the material properties are often nonlinear, adding complexity to the calculations.

The first set of material properties used in early analyses were the ones used by J. Zhu in his 2019 parametric analyses [10] of the **ECRH** reflector tile. The properties included the ones for:

- **Titanium Zirconium Molybdenum** for the reflector tile.
- **Copper Nickel Zirconium** for the heat sink.
- **Stainless Steel 1.4981 X8CrNiMoNb** for the cooling pipe.
- **Sigraflex** for the thermal gasket between the heat sink and the reflector tile.

A few of these material properties were based on outdated sources and needed reevaluation to take into account any change.

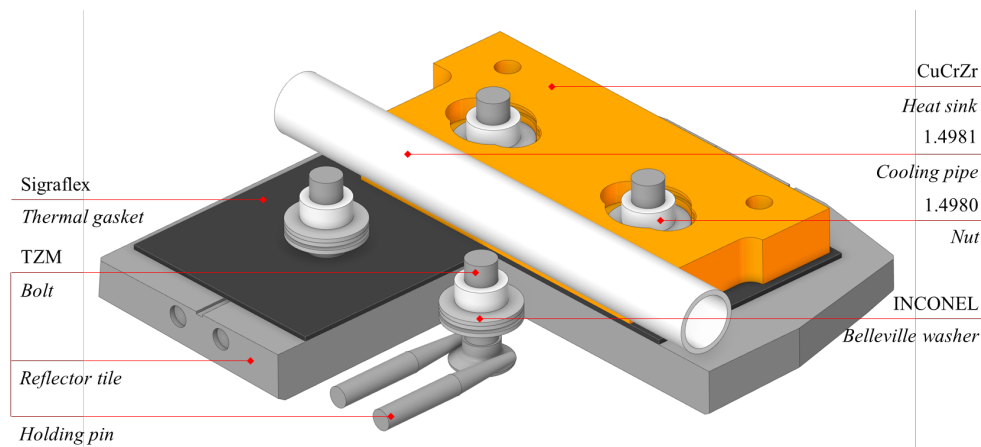


Figure 4.1: Material assignation

The new material properties were set during the project and are split into two big categories, the thermal/physical properties and the mechanical properties. This new set was then saved in an *.xml* file to be ported to other ANSYS Workbench® projects (ie. thermal-structural analysis of **Neutral Beam Injection** target tile).

4.1.1 Thermal properties

Thermal analysis is the main type of analysis done to evaluate the performances and behavior of the **TZM** reflector tile and tile assembly. This is why an accurate modelling of the assembly's constitutive materials is crucial. In addition to the first four materials, the new model should implement the bolting system comprised of **TZM** bolts and holding pins, 1.4980 **X5NiCrTi SS** nuts and 2.4668 Inconel Belleville washers. The bolting system was not included in the 2019 model of J. Zhu [10]. Understanding the impact of such bolting system is important to fully analyse the tile. The complete list for thermal properties is (after update):

- **Titanium Zirconium Molybdenum** for the reflector tile, bolts and holding pins
- **Copper Nickel Zirconium** for the heat sink.
- **Stainless Steel 1.4981 X8CrNiMoNb** for the cooling pipe.
- **Sigraflex** for the thermal gasket between the heat sink and the reflector tile.
- **Stainless Steel 1.4980 X5NiCrTi** for the nuts.
- 2.4668 Inconel for the Belleville washers.

It is also important to note that phenomena such as thermal activation and recrystallization of the alloys are NOT taken into account although finite element analysis could technically support such calculations. The implementation of such physical phenomena would require more material data and more resources in order to correctly model them. It was simply decided to avoid (*if possible*) reaching the recrystallization temperatures of the different part material (in particular the maximum temperature of the **CuCrZr** heat sink since it is the part that would overheat [10, 4]).

4.1.2 Mechanical properties

Mechanical analysis is the second analysis type that will be carried out to evaluate the structural integrity of the reflector tile assembly. Structural analyses are more complex than thermal analyses and require most computing power. They also heavily depend on the meshing and the modelling of the material (ie. plasticity, elasticity) can greatly influence the results. This is why the choice of the material model is pertinent. In his 2019 study, J. Zhu analyzed the fatigue cycle of the reflector tile assembly [10]. The fatigue criteria will not be used in this study.

Hardening and plasticity of the material will only be used in special cases (notably for the **CuCrZr** alloy) to assess the plastic deformation of the parts. For most, the hardening law will be perfectly plastic (tangent modulus = 0 [*GPA*]) and it was assumed (as a first approach) that the parts shouldn't deform plastically.

After reading different datasheets and suppliers data, the mechanical properties were reevaluated and condensed into a new revised material database. For the **Stainless Steel 1.4981 X8CrNiMoNb** of the cooling pipe, the mechanical properties were not given and another similar alloy, in particular 1.4435, was used for its mechanical properties ONLY. For other materials such as **Sigraflex**, the material data was very limited for lack of supplier's data of a better characterization of it.

The updated thermal and mechanical properties of the materials are given in tables.

T	λ	α	C_p	E	ν	ρ
[°C]	[W m ⁻¹ °C ⁻¹]	[°C ⁻¹]	[J kg ⁻¹ °C ⁻¹]	[GPa]	—	[kgm ⁻³]
20	-	5,30E-06	-	300	0,32	10200
25	122	-	248	-	-	-
100	121	-	255	-	-	-
200	119	5,30E-06	264	-	-	-
400	116	5,40E-06	279	-	-	-
500	-	-	-	260	0,32	-
600	112	5,60E-06	289	-	-	-
800	109	5,80E-06	299	-	-	-
1000	-	6,00E-06	-	220	0,32	-
1200	-	6,20E-06	-	-	-	-
1400	-	6,40E-06	-	-	-	-
1500	-	-	-	140	0,32	-
2000	-	-	-	40	0,32	-

Table 4.1: Thermal and mechanical properties of **Titanium Zirconium Molybdenum**

T	λ	α	C_p	E	ν	ρ
[°C]	[W m ⁻¹ °C ⁻¹]	[°C ⁻¹]	[J kg ⁻¹ °C ⁻¹]	[GPa]	—	[kgm ⁻³]
20	338	1,57E-05	388	128	0,3	8920
100	342	1,63E-05	392	125	0,3	-
200	350	1,70E-05	400	121	0,3	-
300	360	1,76E-05	410	115	0,3	-
400	372	1,82E-05	422	109	0,3	-
500	387	1,86E-05	437	102	0,3	-
600	404	1,88E-05	454	-	-	-
700	423	1,90E-05	473	-	-	-

Table 4.2: Thermal and mechanical properties of **Copper Nickel Zirconium**

T	λ	α	C_p	E	ν	ρ
[°C]	[W m ⁻¹ °C ⁻¹]	[°C ⁻¹]	[J kg ⁻¹ °C ⁻¹]	[GPa]	-	[kgm ⁻³]
20	13,5	1,61E-05	472	196	0,3	8010
100	14,9	1,67E-05	501	190	0,3	-
200	16,7	1,72E-05	525	182	0,3	-
300	18,3	1,77E-05	532	174	0,3	-
400	19,8	1,81E-05	555	166	0,3	-
500	21,3	1,84E-05	582	158	0,3	-
600	22,7	1,88E-05	604	150	0,3	-
700	24,2	1,91E-05	610	142	0,3	-
800	25,6	1,94E-05	611	134	0,3	-
900	-	1,97E-05	615	-	-	-
1000	-	2,00E-05	641	-	-	-

Table 4.3: Thermal and mechanical properties of Stainless Steel 1.4981

T	λ	α	C_p	E	ν	ρ
[°C]	[W m ⁻¹ °C ⁻¹]	[°C ⁻¹]	[J kg ⁻¹ °C ⁻¹]	[GPa]	-	[kgm ⁻³]
20	15	1,70E-05	460	211	0,3	8000
100	-	1,70E-05	-	206	0,3	-
200	-	1,75E-05	-	200	0,3	-
300	-	1,78E-05	-	192	0,3	-
400	-	1,80E-05	-	183	0,3	-
500	-	1,82E-05	-	173	0,3	-
600	-	1,85E-05	-	162	0,3	-

Table 4.4: Thermal and mechanical properties of Stainless Steel 1.4980

T	λ	α	C_p	E	ν	ρ
[°C]	[W m ⁻¹ °C ⁻¹]	[°C ⁻¹]	[J kg ⁻¹ °C ⁻¹]	[GPa]	—	[kgm ⁻³]
20	12	1,34E-05	440	199	0,31	8200
100	13	-	-	195	0,31	-
200	-	1,34E-05	-	190	0,31	-
300	-	1,38E-05	-	185	0,31	-
400	-	1,41E-05	-	179	0,31	-
500	19	-	-	174	0,31	-
600	-	1,47E-05	-	167	0,31	-
700	23	-	-	163	0,31	-
800	-	1,64E-05	-	149	0,31	-
900	27	-	-	134	0,31	-
1000	-	-	-	120	0,31	-
1100	-	-	-	100	0,31	-

Table 4.5: Thermal and mechanical properties of INCONEL 2.4668

T	λ_X	$\lambda_{Y,Z}$	α_X	$\alpha_{Y,Z}$	C_p	E	ν	ρ
[°C]	[W m ⁻¹ °C ⁻¹]	[W m ⁻¹ °C ⁻¹]	[°C ⁻¹]	[°C ⁻¹]	[J kg ⁻¹ °C ⁻¹]	[GPa]	—	[kgm ⁻³]
20	3	154	3,00E-05	1,00E-06	700	0,7	0,15	1000
250	2,6	105	-	-	-	-	-	-
500	2,1	82	-	-	-	-	-	-
750	2,1	69	-	-	-	-	-	-
1000	2,1	61	-	-	-	-	-	-
1250	2,1	56	-	-	-	-	-	-
1500	2,1	53	-	-	-	-	-	-
2000	2,1	51	-	-	-	-	-	-

Table 4.6: Thermal and mechanical properties of Sigraflex

4.2 CONTACT CONFIGURATION

The ECRH TZM reflector tile is an assembly composed of different parts held together using a specific bolting system. It is crucial to correctly set the contacts of the parts to accurately model the real life phenomena. Contacts are a quite complex concept and introduce lots of different problematics when modelling them. They can have all sorts of properties such as the number of degrees of freedom and possible movement or a specific heat transfer coefficient. In the case of the reflector tile assembly, the contact are of different types, mainly unidirectional and bonded.

Mathematically, contacts such as unidirectional contacts introduce discontinuities and nonlinearities that can influence convergence of the calculations. The methods chosen for the contacts will impact the speed and stability of the calculations, this is why the settings of the contacts were chosen with great care to avoid faulty calculations and improbable results.

In real life, the TZM tile is placed on top of the Sigrafex thermal gasket. The CuCrZr heat sink is placed in the other side of the Sigrafex thermal gasket. Those two contacts (tile/thermal gasket and thermal gasket/heat sink) are all unidirectional and frictional. The SS cooling pipe is brazed onto the CuCrZr heat sink. This bonds the heat sink and the cooling pipe together. For this contact, it is assumed that both are thermally perfectly bonded, meaning that the temperature on one part at the boundary is the same as the temperature on the contact boundary of the other part. In some cases, this brazed contact will have a reduced contact area to simulate a "bad" brazing and assess the impact of a worsen thermal contact.

The bolting system is a complex assembly and interacting parts composed of the TZM bolts, the TZM holding pins, the SS nut, the INCONEL Belleville washers. The reflector tile has a closed plasma-facing surface. The bolts thus need to be held in the tile, and because it is not possible to directly use the reflector tile to fix the bolt. It was decided to design TZM holding pins screwed on the side of the reflector tile. Those holding/retaining pins are designed to retain the head of the bolt using fingers. In total, 8 of such pins are assembled in the reflector tile. The holding pin/reflector tile connection is threaded but it was deemed acceptable to consider it bonded. The contact between the holding pins and the bolts are, however, unidirectional and frictional. The contact nut to bolt is also threaded but is considered bonded in the model. To accommodate for possible thermal expansion and deformation of the parts while still assuring thermal contact between the TZM reflector tile and the CuCrZr heat sink, as stack composed of three INCONEL Belleville washers acting as a spring, putting pressure on the reflector tile and maintaining thermal contact. The washers push on the CuCrZr heat sink. All those contacts (nut/washer, and washer/heat sink) are considered to be unidirectional and frictional. The contact washer to washer is technically frictional but for modelling and solving reasons, they will be bonded at the outer perimeter, they still can rotate but not move.

4.2.1 Initial contact setup

Initially, the early calculations only included (all contacts bonded):

- The TZM tile
- The Sigrafex thermal gasket.
- The CuCrZr heat sink.
- The SS cooling pipe.

This was done to test the modelling of the tile assembly and the bonding of the parts together. While this wasn't the most accurate model, the thermal calculations didn't need and more complex setup, and for the initial calculations, heat transfer was assumed to be perfect. The idea was then to add the bolting system. This means that the complex mechanical interaction between the bolting parts, especially the stack of Belleville washers needed to be modelled. A global assembly model was thus developed to implement the bolting system on the nature

of the contacts and the modelling choices stated earlier.

It is now possible to establish a contact model for the whole assembly:

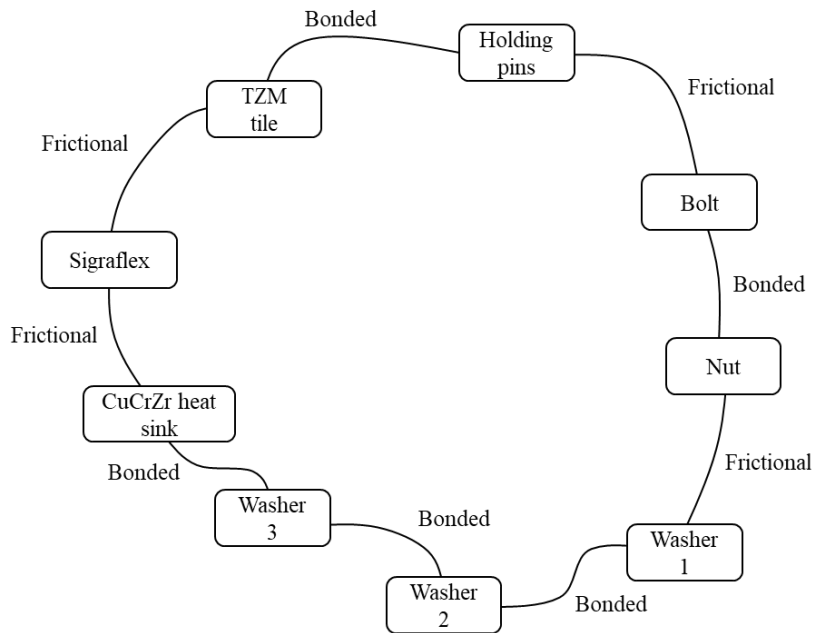


Figure 4.2: *Contact configuration for thermal and structural analysis*

This model is acceptable but will be sometimes modified to assess the impact of the contact modelling.

When setting up the contacts in ANSYS®, it is important to check for gaps or penetrations to avoid clipping issues. The status of the contact on a flat surface to surface contact should be consistent to avoid solving issues.

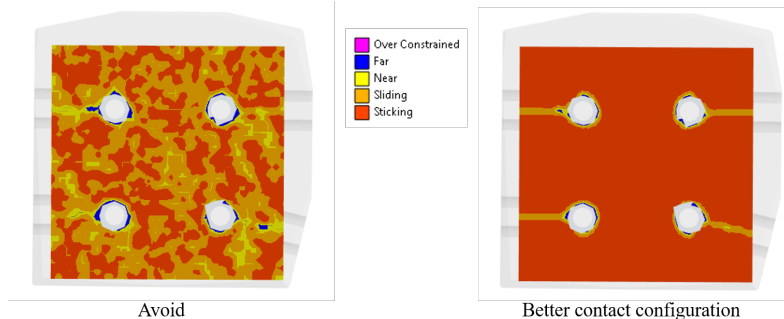


Figure 4.3: *Contact status comparison*

Such inconsistent contacts can make the calculation unstable and potentially prevent

good results. Contact offset can be used to "*close*" the gap of the contacts allowing a better contact configuration. Contact methods can also be modified to other formulations all having their own use cases. For bonded contact and frictional contact, programmed controlled is most used. MPC can also be used for bonded contact, it usually blocks all degrees of freedom using constrain equations. Thermal contact is considered perfect because of the brazing. It is assumed that the heat conduction is really high and the modelling is not possible without data.

4.2.2 Field coupling and contact configuration

Contact are complex phenomena that can be dependant on multiples fields. In the case of thermal-structural analysis, temperature and displacement fields can have an influence on the contact status of a given contact (ie. the break of contact preventing heat conduction). In chapter 5.4, field coupling is used to model the loss of contact between the heat sink and the Sigraflex. It is discussed how manual update of the contact configuration can be of use to assess the need for full field coupling. In the case of too complex

For coupled field calculations (ie. thermal-structural), the elements used have more degrees of freedom (in this case these are displacement and temperature). The problem becomes large and convergence issues arise. It was decided to remove the bolting system as a first approach. The bonding of the **Sigraflex** thermal gasket and the **CuCrZr** heat sink was done in order to simplify the model and allow better if not convergence at all.

4.3 PLASMA HEAT LOAD

The main heat load on the ECRH reflector tile is the plasma heat load. This reflector tile is directly exposed to the plasma. The magnitude of the thermal load depends greatly on the position of the components relative to the plasma. Components in direct contact with the plasma boundary, such as the divertor targets are loaded primarily through convected power loads, whilst the other components such as the wall panels are primarily loaded by radiation from the plasma. For the design of the PFCs it is important to know for the different plasma scenarios how the heating is split between the different components and how it is divided between convected and radiated fractions. In addition to the plasma heat load, the ECRH beam will also contribute to a certain amount to the heating of the tile assembly. Because this assembly going to be under high functional heat loads, it is important to correctly model the heat load of the plasma on the ECRH reflector tile.

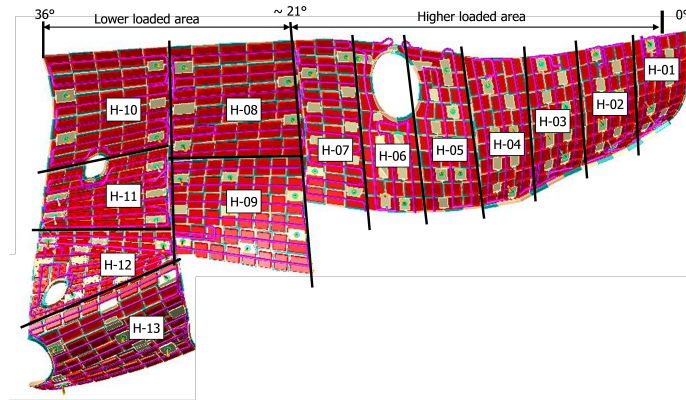


Figure 4.4: *Modules of the heat shield (HS)*

The reflector tile is located in the module ($H - 02$) which is one of the most thermally loaded areas of the HS. The Average thermal load in this area is 250kWm^{-2} [3].

4.4 MODELLING OF THE ECRH BEAM

One of the most crucial aspect of this task is the modelling of the **ECRH** beam. The correct modelling of this beam will help accurately model the real-life stray radiation of the beam.

4.4.1 Calculation of the integration coefficients

The issue was in the parameters of the **ECRH** beam load distribution since it was not clearly defined in the recalculation task requested by Torsten Stange. The little information about the parameters of the beam load were the nominal total heat flow of 912W, Gaussian shape of power distribution and the geometric properties of both axisymmetric and non-axisymmetric distribution. Based on these data, a series of calculations aiming to recalculate the load distribution on the tile surface were undergone and provided good results.

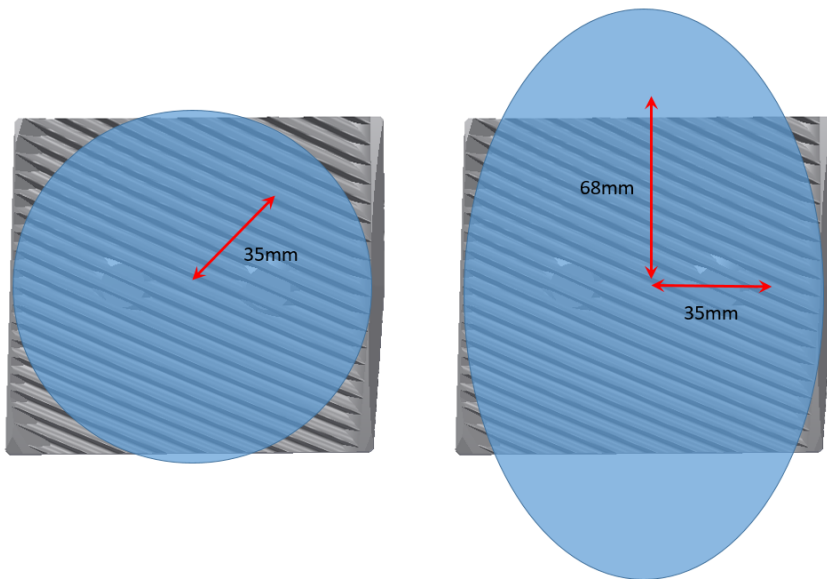


Figure 4.5: Representation of the two *ECRH* beam heat flux distribution cases

The calculation of the integral parameters as well as the analytical calculation of the surface integrals were done on Wolfram Mathematica®. There are two different cases, one axisymmetric (circular) and another non-axisymmetric (elliptical). For the first case, almost all of the power 99% hits the *ECRH* reflector tile. The standard deviation is defined to be 35mm, for debug and validation purposes, 86% of the power should be included within a disk of radius 35mm. For the elliptical distribution, much less power hits the reflector tile. The distribution properties are also different and feature two different radii, the minor semi-radius and the major semi-radius. Their values are respectively 35mm and 68mm, both of them defining an ellipse. Similarly to the circular distribution, for debugging, 86% of the overall power should be included within the area of the ellipse.

With help of those information, the integration coefficients could be calculated. The first integral was expressed in a cylindrical coordinate system. The first APDL code written by J. Zhu [10] in 2019 only featured the circular heat flux distribution and was based on calculations made by Torsten Stange. The integrated function for Gaussian distribution has the form $\exp(-2r^2)$. The surface integral can be written:

$$\int_{\Omega} \exp(-2r^2) dS \quad (4.1)$$

in cylindrical coordinates, $dS = rdrd\theta$ and Ω a surface in \mathbb{R}^2 . When taking the normal distribution, is it possible to rewrite the function and include the standard deviation r_0 . The integral \mathbb{I} of f on Ω is:

$$\mathbb{I}_{\Omega}^f = \int_{\Omega} \exp\left(-2\left(\frac{r}{r_0}\right)^2\right) dS \quad (4.2)$$

When developing the differential (in cartesian coordinates), the integral becomes:

$$\int_{\Omega} \exp\left(-2\left(\frac{r}{r_0}\right)^2\right) dS = \int_0^{+\infty} \int_0^{2\pi} \exp\left(-2\left(\frac{r}{r_0}\right)^2\right) rdrd\theta \quad (4.3)$$

$$\int_0^{+\infty} \int_0^{2\pi} \exp\left(-2\left(\frac{r}{r_0}\right)^2\right) rdrd\theta = \int_0^{+\infty} \exp\left(-2\left(\frac{r}{r_0}\right)^2\right) rdr \int_0^{2\pi} d\theta \quad (4.4)$$

$$= 2\pi \int_0^{+\infty} \exp\left(-2\left(\frac{r}{r_0}\right)^2\right) rdr \quad (4.5)$$

When calculated, the value of this integral is:

$$2\pi \int_0^{+\infty} \exp\left(-2\left(\frac{r}{r_0}\right)^2\right) rdr = 6,125 \cdot 10^{-4} \pi \quad (4.6)$$

This function is then normalized by multiplying both side by a coefficient k_{norm} such as $k_{norm} \cdot 6,125 \cdot 10^{-4} \pi = 1$. This coefficient has a value of $519,69 \text{ m}^{-2}$. Since heat flux is in $[\text{W m}^{-2}]$, k_{norm} needs to be in $[\text{m}^{-2}]$. To validate the normalization, it is possible to integrate the same function, but only for the radius between 0 and standard deviation and multiplying the function by k_{norm} . This gives:

$$k_{norm} \left[\int_0^{r_0} \int_0^{2\pi} \exp\left(-2\left(\frac{r}{r_0}\right)^2\right) rdrd\theta \right] = 0,8646 \quad (4.7)$$

The integral power of the ECRH beam is 912 W. This means that normalized ECRH beam power distribution can be multiplied by the integral power. It is thus possible to define $q_0 := P_{ECRH}^{beam} \cdot k_{norm}$. In the case of the circular ECRH Gaussian heat flux distribution, the value of $q_0 = 473957 \text{ W m}^{-2}$, this value will be used in the APDL code. The implemented function is, in cylindrical coordinates (4.9):

$$f_{axisym.}^{cyl.CS}(r) = P_{ECRH}^{beam} k_{norm} \exp\left(-2\left(\frac{r}{r_0}\right)^2\right) [\text{W/m}^2] \quad (4.8)$$

$$f_{axisym.}^{cyl.CS}(r) = 473957 \exp\left(-2\left(\frac{r}{35[\text{mm}]}\right)^2\right) [\text{W/m}^2] \quad (4.9)$$

For the cartesian coordinates, the method of normalization is analog to the method used for the integral normalization in cylindrical coordinates. The choice of the cartesian coordinate system is because of the function for the elliptical ECRH power distribution case and the way the ellipse is defined. Although it is possible to vary the radius in function of the angle while working in cylindrical coordinates, or use the ellipse equation and application of Fubini's theorem in cartesian coordinates, another more practical approach was used to compute the integral. The function f written in cartesian coordinates is as follows (a is the minor semi-radius and b is the major semi-radius):

$$f(x,y) = \exp\left(-2\left(\left(\frac{x}{a}\right)^2 + \left(\frac{y}{b}\right)^2\right)\right) \quad (4.10)$$

The integral of the function over Ω is written:

$$\mathbb{I}_{\Omega}^f = \int_{\Omega} \exp\left(-2\left(\left(\frac{x}{a}\right)^2 + \left(\frac{y}{b}\right)^2\right)\right) dS \quad (4.11)$$

in cartesian coordinates, $dS = dx dy$ and Ω a surface in \mathbb{R}^2 . For the moment, the function (4.10) is integrated over \mathbb{R}^2 . To normalize the integral, it is possible to proceed the same way than for the cylindrical integral (4.2).

$$\int_{\mathbb{R}^2} \exp\left(-2\left(\left(\frac{x}{a}\right)^2 + \left(\frac{y}{b}\right)^2\right)\right) dS = \int_{-\infty}^{+\infty} \int_{-\infty}^{+\infty} \exp\left(-2\left(\left(\frac{x}{a}\right)^2 + \left(\frac{y}{b}\right)^2\right)\right) dx dy \quad (4.12)$$

If a and b are equal, the distribution is circular. The normalization coefficient for the cartesian should therefore be the same as the cylindrical one since the standard deviation of the distribution is the same, the function is just expressed in a cartesian coordinate system. Let $a = b = 35\text{mm}$, the integral becomes:

$$\int_{-\infty}^{+\infty} \int_{-\infty}^{+\infty} \exp\left(-2\left(\frac{x+y}{35[\text{mm}]}\right)^2\right) dx dy = 6,125 \cdot 10^{-4} \pi \quad (4.13)$$

The normalization coefficient is $519,69 \text{ m}^{-2}$ and the integration coefficient $q_0 = 473957 \text{ W m}^{-2}$. This coefficient is the same as the one for the distribution expressed a cylindrical coordinates. To validate this, it possible to proceed the same as with the cylindrical distribution, integrating over a disk of radius 35 mm . There is a problem with integrating the function on a circle in Cartesian coordinates, because the surface is a square of a rectangle. It is however possible to find an alternative solution to this problem using the Heaviside step function. The 2D-Heaviside step function is a discontinuous function defined as follows:

$$H_{\Omega}(x,y) = \begin{cases} 1 & \text{if } (x,y) \in \Omega \\ 0 & \text{if } (x,y) \in \mathbb{R} \setminus \Omega \end{cases} \quad (4.14)$$

The idea to calculate the integral over a circle or an ellipse is to multiply the integrated function by the Heaviside function (4.14) to project its values over a non-zero area defined by $\partial\Omega$, the closed perimeter of the surface.

The domain on which it is necessary to integrate is bounded by the circle equation $x^2 + y^2 = r_0^2$. Because the domain is a disk, the equation becomes $x^2 + y^2 \leq r_0^2$. The domain of the circle is thus $\Omega = \{(x,y) \in \mathbb{R}^2, r_0 \in \mathbb{R} : r_0^2 - x^2 - y^2 \geq 0\}$ and by the way the Heaviside

step function (4.14) is defined in Wolfram Mathematica®, it becomes $H(r_0^2 - x^2 - y^2)$.

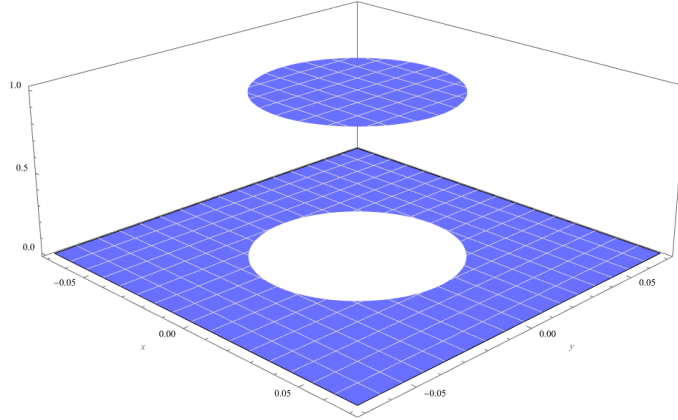


Figure 4.6: 3D graph of the Heaviside step function defined over Ω

To validate the coefficient $k = 519,69 \text{ m}^{-2}$, it is possible to now integrate in Cartesian coordinates but on a disk. As said previously, the idea is to project the values of a function f on a non-zero area Ω defined by H_Ω , this is written as follows:

$$\int_{\Omega_{cyl}} f r dr d\theta = \int_{\Omega_{car}} \langle f, H_\Omega \rangle dx dy \quad (4.15)$$

with Ω_{cyl} being the cylindrical integration limits and Ω_{car} the cartesian integration limits. The fully written and calculated integral is :

$$k \int_{-a}^a \int_{-b}^b \left\langle \exp \left(-2 \left(\frac{x+y}{35[\text{mm}]} \right)^2 \right), H(35[\text{mm}]^2 - x^2 - y^2) \right\rangle dx dy = 0,867 \quad (4.16)$$

The value of the integral is correct, and the integration coefficient for the Cartesian coordinates heat flux distribution is $q_0 = 473957 \text{ W m}^{-2}$, which is the same as the cylindrical one. This is a good sight since the distribution are defined to be the same, it is reassuring to get the same result. For the elliptical one, the method is the same as the circular one except the argument in the Heaviside step function (4.14) isn't derived for the circle equation but from the ellipse equation. The function for axisymmetric heat flux distribution written in cartesian coordinates is (4.17):

$$f_{axisym}^{car,CS}(x,y) = 473957 \exp \left(-2 \left(\frac{x+y}{35[\text{mm}]} \right)^2 \right) [\text{W/m}^2] \quad (4.17)$$

For the calculation of the non-axisymmetric integration coefficient (semi-minor radius of 35 mm and semi-major radius of 68 mm), it is possible to proceed the same way as above. The ellipse is defined via the ellipse equation $(\frac{x}{a})^2 + (\frac{y}{b})^2 = 1$ with a and b being respectively the minor semi-radius and major semi-radius. The Heaviside step function (4.14) is written $H \left(1 - \left(\frac{x}{a} \right)^2 - \left(\frac{y}{b} \right)^2 \right)$. The normalization of the integral as well as the calculation of the integral on the ellipse is done the same way as before. The function on which the distribution f is projected is the Heaviside step function (4.14) defined on an ellipse. The projection $\langle f, H_\Omega \rangle$ is integrated and the results yields a normalization coefficient k_{norm} of $267,5 \text{ m}^{-2}$

and an integration coefficient q_0 of 243948 W/m^2 . The function for non-axisymmetric heat flux distribution written in cartesian coordinates is (4.18):

$$f_{\text{car.CS}}^{\text{car.CS}}(x, y) = 243948 \exp \left(-2 \left(\left(\frac{x}{35[\text{mm}]} \right)^2 + \left(\frac{y}{68[\text{mm}]} \right)^2 \right) \right) [\text{W/m}^2] \quad (4.18)$$

All integration coefficients as well as the standard deviations of the distributions are summarized below:

<i>Loadcases</i>	<i>Integration coefficient</i>	k_{norm}	<i>Semi-minor axis</i>	<i>Semi-major axis</i>
<i>heat flux distri.</i>	$[\text{W m}^{-2}]$	$[\text{m}^{-2}]$	[m]	[m]
<i>Axisymmetric [cyl. CS]</i>	473957	519,69	0,035	0,035
<i>Axisymmetric [car. CS]</i>	473957	519,69	0,035	0,035
<i>Non – axisymmetric [car. CS]</i>	243948	267,5	0,035	0,068

Table 4.7: ECRH beam gaussian distribution parameters

4.4.2 Coding strategy and implementation in ANSYS®

In ANSYS® Mechanical, the heat flux applies a uniform heat load over the whole boundary. This, of course, could be used to model the ECRH beam on the TZM tile plasma facing surfaces. While possible, this would be too conservative for the results and provide unrealistic data. This is why, a custom heat load is used to model the heat distribution of the ECRH beam. ANSYS® Mechanical does feature an APDL command function that creates an APDL environment where it is possible to write a script that is executed when needed.

This figure shows how the cartesian code works, the original code was written in a cylindrical coordinate system.

After calculating the ECRH beam load distribution function for different cases, the functions need to be implemented in ANSYS®. The code written by J. Zhu [10] in 2019 can be reused and modified to accommodate for coordinate system change. The original code was written in cylindrical coordinates with only one loop for one variable, the radius r . However, the future code should support both axisymmetric and non-axisymmetric distributions, which means having two variables, x and y . First, the code calculated the heat flux following the heat flux distribution functions at the midpoint of this area (4.17)(4.18). The code then selects all elements within a small area and apply to all of them the value of the calculated heat flux from the midpoint of this area.

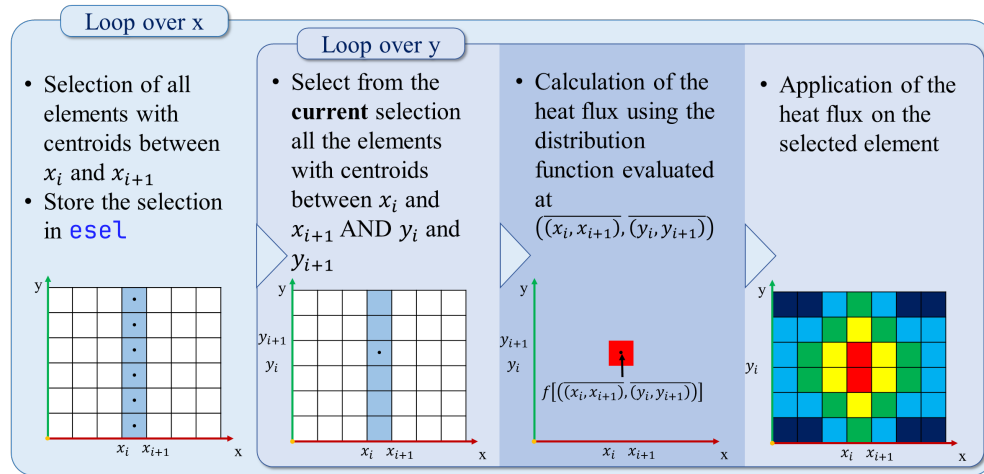


Figure 4.7: Heat flux distribution script for APDL

Listing 1: APDL script of the gaussian heat distribution developed by J. Zhu [10]

```

csys,100
cmsel,s,plasma_srf
esln
esel,r,ename,,152
nsle
cm,temp,elem

cycn=arg3/arg2+1
cycn=nint(cycn)

! -----
*do,n_,1,cycn ! positive
  cm sel,s,temp
  x1=(n_-1)*arg2
  x2=n_*arg2
  x0=(x1+x2)/2

  esel,r,cent,x,x1,x2
  *get,elemn_,elem,0,count
  ! calc the heat flux follow the above formula
  flux_0=-2*(x0/0.05)**2
  flux_x=250000*exp(flux_0)+arg1

  *if,elemn_,ne,0,then
    sfe,all,1,HFLU,1,flux_x
  *endif
*enddo

! -----
alls $ csys,0
kbc,1

```

The code above was developed by J. Zhu for the ECRH beam implementation in ANSYS®. This code was reused to help compare the new code with the existing one. The new code below was developed to support both axisymmetric and non-axisymmetric heat load distribution. The non-axisymmetric distribution is expressed in a cartesian coordinate system, the code should then be rewritten to include a double for-loop, one for each axis. The new code is a little bit longer but can support any distribution. It was tested extensively by calculating the surface integral and comparing the results with the analytical calculations (see 5.1.1).

Listing 2: APDL script of the gaussian heat distribution developed for both axisymmetric and non-axisymmetric

```

csys ,110
cmsel ,s ,plasma_srf
esln
esel ,r ,ename , ,152
nsle
cm ,temp ,elem
cycn=arg3/arg2+1
cycn=nint(cycn)
! -----
*do ,i_ ,1 ,cycn
x1=(i_-2)*arg2
x2=(i_-1)*arg2
x0=(x1+x2)/2i
*do ,j_ ,1 ,cycn
! selection of the temperature
cmsel ,s ,temp
y1=(j_-2)*arg2
y2=(j_-1)*arg2
y0=(y1+y2)/2
esel ,r ,cent ,x ,x1 ,x2
esel ,r ,cent ,y ,y1 ,y2
*get ,elemn_ ,elem ,0 ,count
! calc the heat flux follow the above formula
flux_0=-2*(((x0-0.052067)/0.035)**2)+(((y0
-0.05142)/0.068)**2)
flux_x=243948*exp(flux_0)+arg1
*if ,elemn_ ,ne ,0 ,then
  sfe ,all ,1 ,HFLU ,1 ,flux_x
*endif
*enddo
*enddo
! -----
alls $ csys ,0
kbc ,1

```

5 | ANALYSES SETUP AND RESULTS

In this chapter, the setup of the different analysis is explained and the results are discussed.

5.1 STEADY-STATE THERMAL ANALYSIS

Steady-state thermal analysis is the main type of analysis that was carried out to analyse the different components of the ECRH TZM-reflector tile assembly. Different scenarios and loadcases were designed to give insight on the thermal behavior and performances of the tile, that being, the impact of the design changes of the TZM-reflector tile, the influences of different ECRH beam configurations or the influences of the film coefficient in the cooling pipe.

5.1.1 Calculation of the surface integrales

To compare between the old and new tile design but also validate the finite element model, calculating the surface integral can be of use. This idea behind this is to check for energy conservation after integration the heat flux of the ECRH beam on the tile surface. Analytical calculations are a good approach to estimate the overall heat flow through the TZM tile. After the calculation of the surface integrales (see 4.4), it is possible to numerically estimate an integral and predict the heat flux through the old and the new design.

The surface onto which the heat distribution is integrated is a rough approximation of the surface of the TZM tile (the projected area of the tile was simplified to a rectangle of size $95\text{mm} \times 95\text{mm}$). The function is then integrated using a Wolfram Mathematica® script. To evaluate the validity of the analytical calculation, a finite element model including only the old and the new TZM tile was developed to calculate the surface integral but using the finite element method. The idea is to compare both methods to estimate the heat flow.

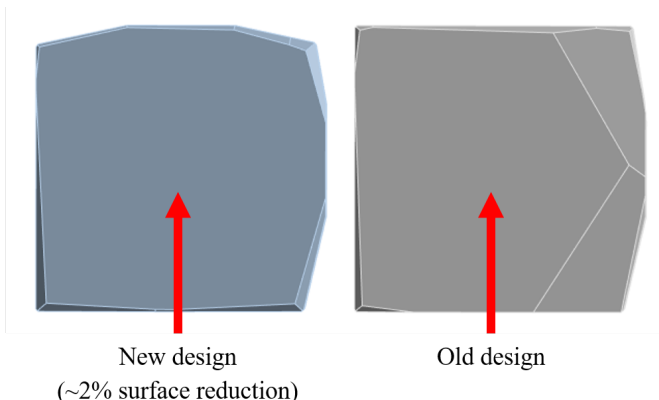


Figure 5.1: 3D model of the TZM tiles for integral calculation

The idea of this analysis is to apply a heat flux on the plasma facing surface and a set temperature (20°C) at the back of the tile. This allows to calculate the power needed to assure (20°C) at the backside of the tile. According to the theory of conductivity, the heat

flow entering the tile should be the same as the heat flow evacuated at the back. This can be calculated analytically using the integral form of Fourier's law. (see 2.3.2)

$$\iint_S \mathbf{q} \cdot d\mathbf{S} = -k \iint_S \nabla T \cdot d\mathbf{S} \quad [\text{W}] \quad (5.1)$$

The left hand side of the equation 5.1 is the thermal power $\partial_t Q$ in [W] transferred by conduction and defined as $\partial_t Q := \iint_S \mathbf{q} \cdot d\mathbf{S}$. The differential $d\mathbf{S}$ is an oriented surface area element in [m^2]. On the right hand side of the equation is surface integral of the dot product between the temperature gradient ∇T and an oriented surface area element $d\mathbf{S}$. To integrate this equation, it is assumed that the material is homogeneous with constant thermal conductivity. It is then possible to integrate 5.1 for a 1-D geometry between two points. The result of the integration gives the following expression for heat flow expression:

$$\partial_t Q = -k \frac{A}{L} \Delta T \quad [\text{W}] \quad (5.2)$$

In this expression, A is the cross-sectionnal area perpendicular to the heat flux in [W], L is the distance between the two surfaces in [m], ΔT is the temperature difference between both front and back surfaces and k is the thermal conductivity of the medium in [W/m^2K]. The cross-sectionnal area A and the length L are assumed constant as well as the thermal conductivity k . It is possible to determine the heat flow flowing through the tile and the heat flow evacuated through the boundary condition, they should be equal to satisfy energy conservation. Based on this, it is possible to use a model to approximate the heat flow through the tile.

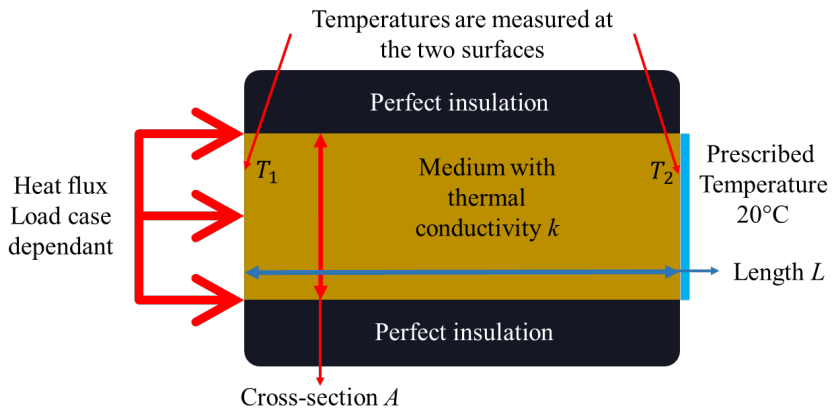


Figure 5.2: Model of the 1-D conduction test

According to 5.2, the evolution of the temperature inside the medium is linear. It is then possible to calculate the heat flow flowing in and out (resp. $\partial_t Q_{in}$ and $\partial_t Q_{out}$). The idea is to find what heat flow $\partial_t Q_{out}$ is needed in order to respect the prescribed temperature boundary condition. After some calculations, it was found that $\partial_t Q_{in} = -\partial_t Q_{out}$. This validates the idea of calculating the surface integral using ANSYS®. The solver settings of the ANSYS® project are by default program controlled. Since the calculation isn't too complex, it is acceptable to continue with these settings. Prescribed temperatures at the back of the TZM tiles were defined and set to 20°C (it is also important to keep in mind that the backside

temperature doesn't affect the value of the integrals, any arbitrary temperature will work).

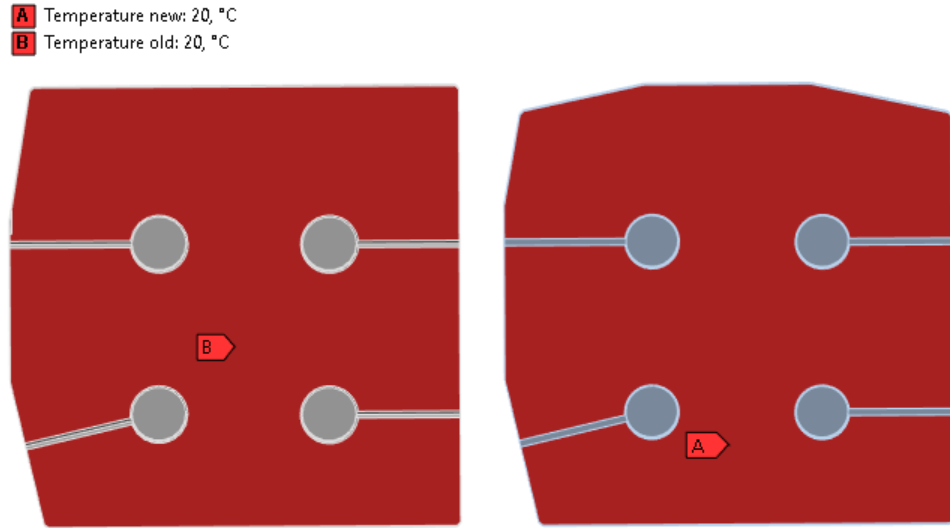


Figure 5.3: Prescribed temperature of the ANSYS® model for surface integral calculations

The loadcases are the standard loadcases chosen to analyse the tile assembly. They were designed to assess the influence of different ECRH beam heat flux distributions on the thermal behavior of the TZM tile. They are:

<i>Load cases</i>	<i>Load case number</i>	<i>Plasma radiation</i>	<i>ECRH heat load</i>	<i>Film coefficients</i>
Plasma rad. ONLY	1	yes	no	$15 \text{ kWm}^{-2\circ}\text{C}^{-1}$
Plasma rad. + ECRH axisym.	2	yes	yes	$15 \text{ kWm}^{-2\circ}\text{C}^{-1}$
Plasma rad. + ECRH non-axisym.	3	yes	yes*	$15 \text{ kWm}^{-2\circ}\text{C}^{-1}$
Plasma rad. + ECRH axisym. [J. Zhu parameters] [10]	4	yes	yes**	$15 \text{ kWm}^{-2\circ}\text{C}^{-1}$

Table 5.1: Simulation scenarios, *non-axisymmetric heat flux distribution, **integration coefficients from J. Zhu [10]

The integral can be calculated analytically on Wolfram Mathematica® for the different load cases. The surfaces of the analytical calculations were simplified (to a rectangle) to avoid too complex calculations. It would have been possible to define a Heaviside over a surface defined by an intersection of different linear functions bounding the domain of the surface. The analytical calculations were done to estimate the order of magnitude of the heat flow through the tile.

<i>Load cases</i>	<i>Surface integral for old design*</i> , [W]	<i>Surface integral for new design**</i> , [W]
Plasma heat load (250 kW m^{-2})	2700,8	2653,0
ECRH axisym. ONLY	912,0	912,0
ECRH non-axisym. ONLY	791,4	791,4
Plasma heat load + ECRH axisym.	3612,8	3565,0
Plasma heat load + ECRH non-axisym.	3492,2	3444,4

Table 5.2: Analytical calculations of the surface integrales, *Old tile surface = $0,010803 \text{ m}^2$, **New tile surface = $0,010612 \text{ m}^2$

The calculation of the surface integrals on ANSYS® will be compared to the analytical results. They will be used as reference values. The calculations are done with different elemental order (linear and quadratic). In general, for thermal calculations, the elemental order is linear as the results wont change much with respect to the order.

<i>Load case</i>	<i>Surface integral for old design, [W]</i>		<i>Surface integral for new design, [W]</i>	
	1mm	2mm	1mm	2mm
<i>Linear elements</i>				
Plasma heat load ONLY	2700,6	2700,6	2652,9	2652,9
Plasma rad. + ECRH axisym.	3608,0	3607,6	3559,4	3560,3
Plasma rad. + ECRH non-axisym.	3495,9	3495,6	3446,8	3447,8
Plasma rad. + ECRH axisym. [J. Zhu parameters] [10]	3612,1	3611,5	3562,2	3562,3
<i>Quadratic elements</i>				
Plasma heat load ONLY	2700,6	2700,6	2652,9	2652,9
Plasma rad. + ECRH axisym.	3607,2	3607,4	3559,4	3560,5
Plasma rad. + ECRH non-axisym.	3495,6	3495,7	3446,9	3447,6
Plasma rad. + ECRH axisym. [J. Zhu parameters] [10]	3611,8	3611,3	3562,2	3562,4

Table 5.3: Finite element calculations of the surface integrales using the model 5.1

There are a few things that can be discussed. Firstly the elemental order doesn't drastically change value of the integral (the value of the integral changes by about 0,1 W between linear and quadratic elements). For the thermal analysis of the whole tile assembly, linear elements will be used to mesh the geometries. Another parameter is the element size that varies between 1 and 2 mm and the variation also doesn't affect the results (the surface integrales vary by about *max.* 1 W). The numerical calculations allow to verify the analytical calculations and show little variation between values with only about 0,08 % variation of heat flow in average between the two calculations methods.

The surface integrales of the two design can also be used to assess the decrease of heat flow through the surfaces.

5.1.2 Comparison between old and new TZM tile design

The surface integrales of the two design can also be used to assess the decrease of heat flow through the surfaces. It is also possible to calculate the energy balance to check the validity of the calculation. Analytically, it is already possible to see the decrease in power flow through the tile. This approximately 1,7 % decrease in power flow is in accordance to the 2 % surface area decrease. The geometry change does have the desired effect.

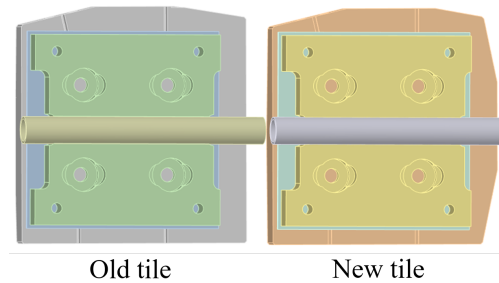


Figure 5.4: Prescribed temperature of the ANSYS® model for surface integral calculations

The four load cases (see table 5.1) were calculated for the tile assembly. The radiation on the plasma-side and PV-side of the TZM tile as well as the CuCrZr heat sink and SS cooling pipe is applied.

The calculations are done and the reaction of the boundary conditions is calculated and summed ($\Sigma Power_{out}$) and compared to the FE calculations. So it is possible to validate the numerical model:

Load cases	Surface integral, [W]	$\Sigma Power_{out}$, [W]
Plasma heat load (250 kWm ⁻²)	2652,9	2652,9
Plasma heat load + ECRH axisym.	3560,3	3559,8
Plasma heat load + ECRH non-axisym.	3447,8	3450,4
Plasma rad. + ECRH axisym. [J. Zhu parameters] [10]	3562,3	3562,2

Table 5.4: Power conservation summary table

The calculation of the whole tile assembly provided good insight on the temperature distribution within the TZM tile and the CuCrZr heat sink. It is possible to see the temperature reduction as an effect of a lower exposed surface area of the TZM tile. The temperature of the heat sink is also lower for the new design than the older one. The design change of the TZM reflector tile thus have an effect on the temperature fields of the assembly parts. **It is also important to keep in mind that the convection coefficient is set to $30 \text{ kW m}^{-2} \text{C}^{-1}$, which is not realistic.** This was assumed to compare the old calculations with the new model.

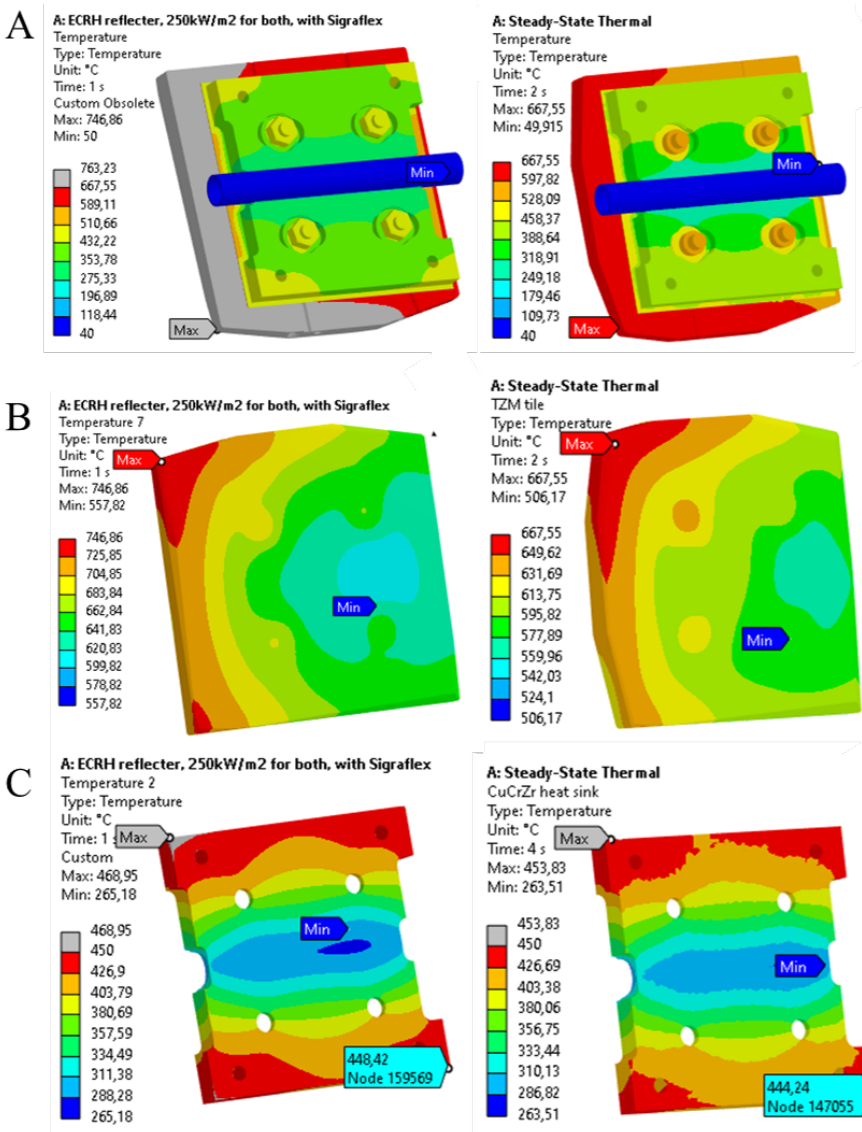


Figure 5.5: Temperature fields for resp. old and new design. Viwa A is the entire model, view B is just the TZM reflector tile and view C is the CuCrZr heat sink.

The power conservation is indeed respected and it is possible to conclude several points:

- The power conservation is respected and validates the numerical model.

- The analytical and numerical calculations show that the new design (reduction of the **TZM** tile surface area) reduced power flow through the assembly by about 1,85 % the initial power of the plasma heat load (**ECRH** heat flux being small near the edges of the **TZM** tile, it doesn't affect much the integral heat flow).
- The new design also lowered the temperature of all assembly parts, especially the **Cu-CrZr** heat sink with a decrease of about 3,33 % of initial design temperature.

5.1.3 Film coefficient influence on thermal behavior

After calculating the surface integrales, it is possible to perform the thermal analysis for the different film coefficients to assess the influence of it on the temperature field inside of the assembly parts. The calculations were performed used the model defined in chapter 3.1. Early calculations without **ECRH** heat load showed non-negligible influence of film coefficient variations on thermal behavior of the **TZM** reflector tile assembly. The film coefficient's value was swept and only the lowest and highest were graphed as they are the most interesting points.

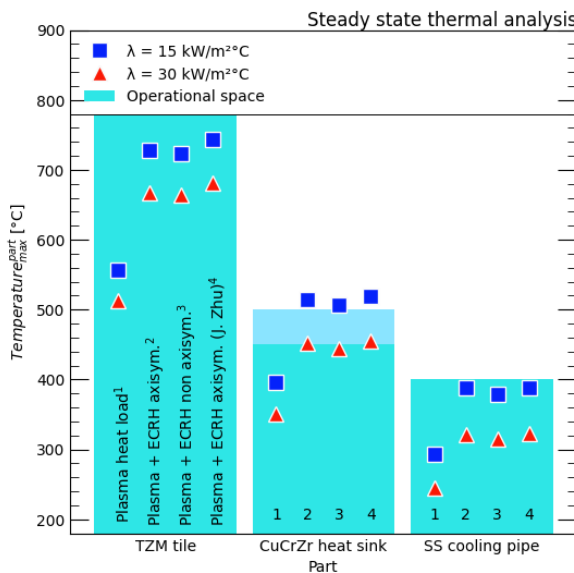


Figure 5.6: Maximum part temperature in function of load case. The maximum operational temperature is not fixed for **CuCrZr**.

It is possible to assess the temperature differences on the temperature fringe of the ANSYS® Mechanical post-processor. The lowest film coefficient (the one most likely to be attained during operation) is not enough to keep the heat sink from overheating (if said maximum operational temperature of **CuCrZr** is set to 450 °C). Another temperature limit discussed with Axel Lorenz was set to 500 °C (after the **CuCrZr** was tested at the Karlsruhe Institute for Technology and no signs of considerable damage was seen).

The maximum temperature of the heat sink at $15 \text{ kW m}^{-2}\text{°C}$ exceeds the maximum temperature of 450 °C [4] [10] by about 13,7 % (511,67 °C). If the maximum temperature was set to be 500 °C, the lowest film coefficient still wouldn't allow 250 kW m^{-2} . **It is possible to conclude that the film coefficient range stated by J. Fellinger is not enough to keep the heat sink from overheating/recrystallizing.**

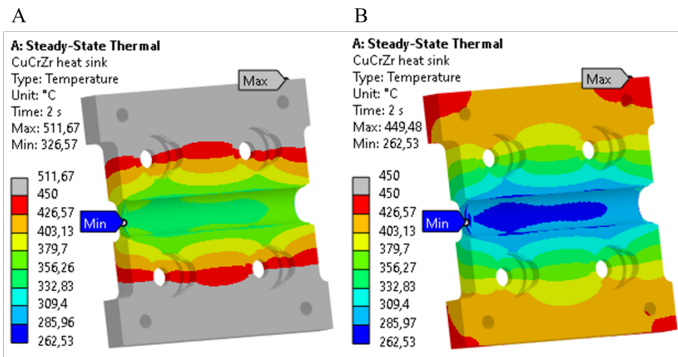


Figure 5.7: Maximum heat sink temperature for two film coefficients. View A is the old TZM reflector tile design's heat sink and view B is the new TZM reflector tile design's heat sink

5.1.4 Load case influence on thermal behavior

To gain more insight on the thermal behavior of the tile assembly and characterize its functioning, it is possible to perform static thermal analysis for various load cases, namely the load cases explained in table 5.1.2. The film coefficient used fore these calculations is the low $15 \text{ kW m}^{-2} \text{ }^\circ\text{C}$.

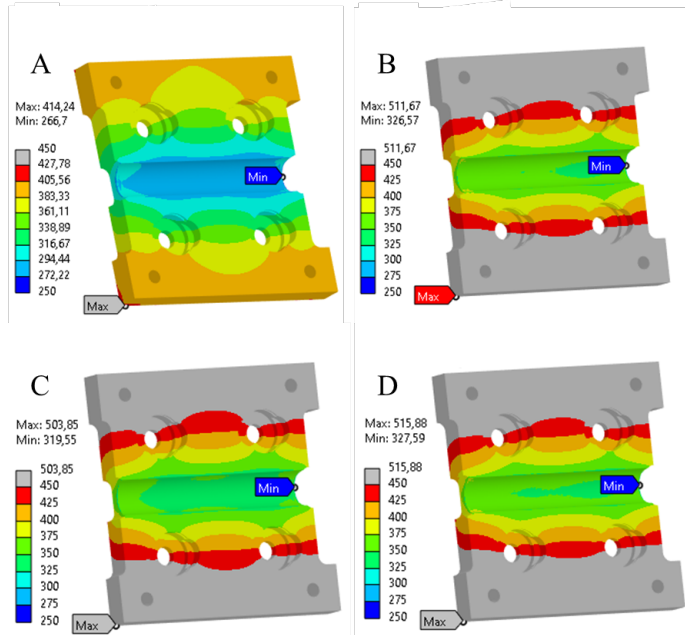


Figure 5.8: Maximum heat sink temperature in function of load case. View A is for plasma heat load ONLY case, View B is for plasma heat load + ECRH axisymmetric heat load, View C is for plasma heat load + ECRH NON-axisymmetric heat load and View D is for plasma heat load + ECRH axisymmetric heat load with J. Zhu parameters.

For the first case, there is no overheating of the heat sink. For the three other cases, the heat sink overheats with the last case (the ECRH heat load with the parameters from J. Zhu) being the worst with the highest maximum temperature. In all cases with ECRH beam on, a big fraction of the heat sink exceeds the maximum operational temperature. The issue of the recrystallization of the bronze alloy was discussed and deemed NOT necessarily problematic since the temperature of 450 °C can be exceeded and it was stated during a discussion with Axel Lorenz that the alloy can be used beyond this temperature. While it is possible to simulate accurate metallurgical phase changes, it is nonetheless complicated to model due to lack of metallurgical and thermodynamical properties.

Because this analysis is a static analysis, the temperature field satisfies the thermal equilibrium equation $0 = -\alpha \nabla T$. It is possible to perform a transient thermal analysis to determine the critical time at which temperature is exceeded for the ONE of the parts and check the evolution of the temperature field for different pulse durations.

5.2 TRANSIENT THERMAL ANALYSIS

Transient thermal analysis is carried out to assess the different time duration at which:

- the maximum operational temperature of the parts is exceeded.
- the thermal equilibrium is attained.
- the effect of high temperature gradient on the evolution of the part temperature.

Those points will help us better understand the thermal behavior of the tile and maybe allow to set time constraints on pulse duration to avoid damaging the assembly.

5.2.1 Analysis for HE1 to HE4 pulse duration

During the operational life W7-X, the device will be used in different operational phases. Each operational phase has different and specific operational parameters such as the plasma pulse duration [8]. The plasma pulse duration are called *HE* and have a number to characterize them. There are 5 different pulse length (noted *HE1* to *HE4*).

Pulse cycles for thermomechanical layout (minimum requirements)					
Heating energy stages	HE1	HE2	HE3	HE4	HE5
Maximum power per pulse [MW]		10			24
Plasma pulse duration [s]		10			10
Energy per pulse [MJ]		100			240
Pulses per day / Dwell time	30 / 900			30 / 900	
Plasma pulse duration [s]	100	200	600	1800	
Energy [GJ] per Pulse	1	2	6	18	
Pulses per day		1			
Imparted energy per day [GJ]	4	5	9	21	7,2

Figure 5.9: Table of the pulse durations [8]

For OP2, the next operation phase of W7-X, the next pulse duration is *HE2* (in an ideal case, the parts of the tile assembly should not exceed their maximum temperature). The tile assembly will be simulated for all cases except *HE5*. The pulse is modelled by a step function and the boundary conditions are the same as the one for the static thermal analysis 5.1.4.

It is also important to calculate a minimum timestep to avoid calculation errors. For this, it is necessary to set a Fourier number and use its definition to calculate the minimum timestep. We set the Fourier number Fo to be 10 (enough time has passed to the tile to reach equilibrium temperature). It is important to note that this number is a placeholder and is assumed to be that value.

The solver is set for 5 loadsteps:

- Loadstep 1 is the initial pulse start with small timesteps.
- Loadstep 2 is the HE1 pulse (100s).
- Loadstep 3 is the HE2 pulse (200s).
- Loadstep 4 is the HE3 pulse (600s).
- Loadstep 5 is the HE4 pulse (1800s).

With that in mind, it is possible to run the calculations. The way the results are calculated is by dividing the maximum temperature of the parts by their respective maximum operational temperature. This allows to measure the distance between the maximum temperature and the operational temperature. When the maximum temperature exceeds the operational temperature, it is also possible to know when (when the ratio is equal to 1) and how much.

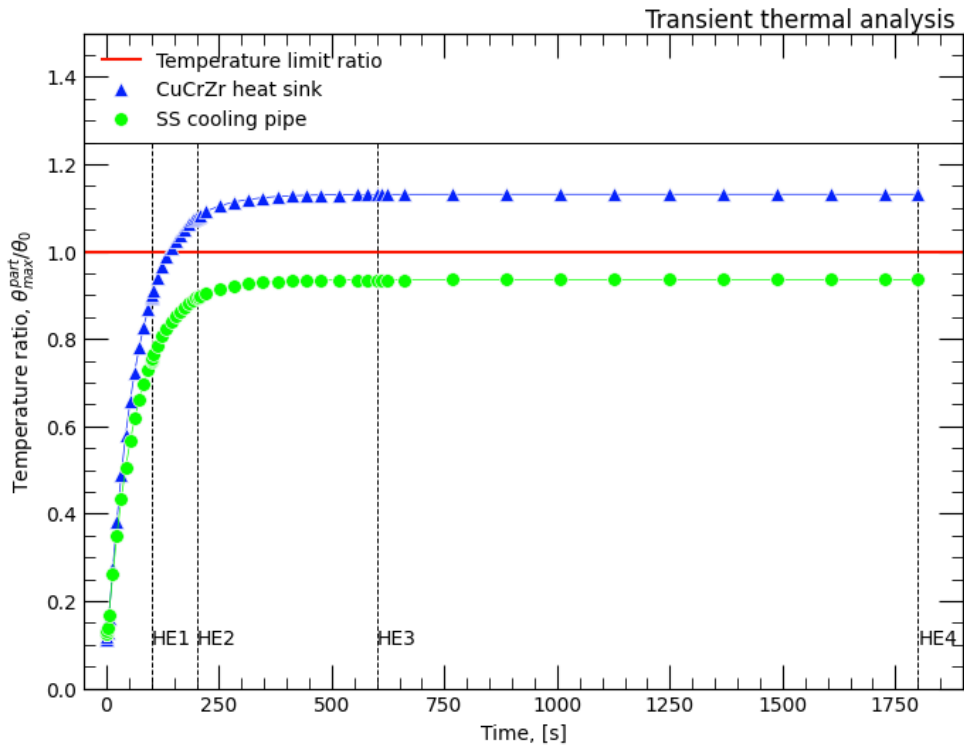


Figure 5.10: Evolution of the temperature ratio $\frac{\theta_{\text{max}}^{\text{part}}}{\theta_0}$ in function of time (with echelon at all HE pulse steps). Calculation done for the load case : Plasma heat load + ECRH axisymmetric heat load.

It is nonetheless important to keep in mind that technically, the maximum temperature

of the heat sink change with respect to the stress, this analysis being entirely thermal doesn't take this into account. It is now possible to conclude on several different points

- The **CuCrZr** heat sink attains and exceeds maximum operational temperature **143 s** after pulse start.
- For **HE2**, the temperature of the heat sink is exceed by about $1.08 \times$ the max. allowable temperature (450°C).
- Quasi-steady-state is reached about 250 s after pulse start.
- **The heat sink doesn't respect specifications if max. CuCrZr operational temperature is 450°C .**

5.2.2 Analysis for HE1 pulse length and cooldown

Because of the nature of heat transfer, for short duration, high heat fluxes, the heat wave travels at a certain speed, causing temperature increase **after** shutdown of the heat load. This latent heat diffusion effect was seen by Vojtěch Smolík and the **NBI** dump tile. The heat load was 10 MW m^{-2} during a fraction of a second. At this heat flux, the heat wave would heat the heat sink even after shutdown of the **NBI**. To assess this effect of latent heating, the **ECRH** reflector tile will be exposed to **HE1** pulse duration (100 s) with 300 s of cooldown. This transient analysis will help assess the magnitude of the latent heating phenomena.

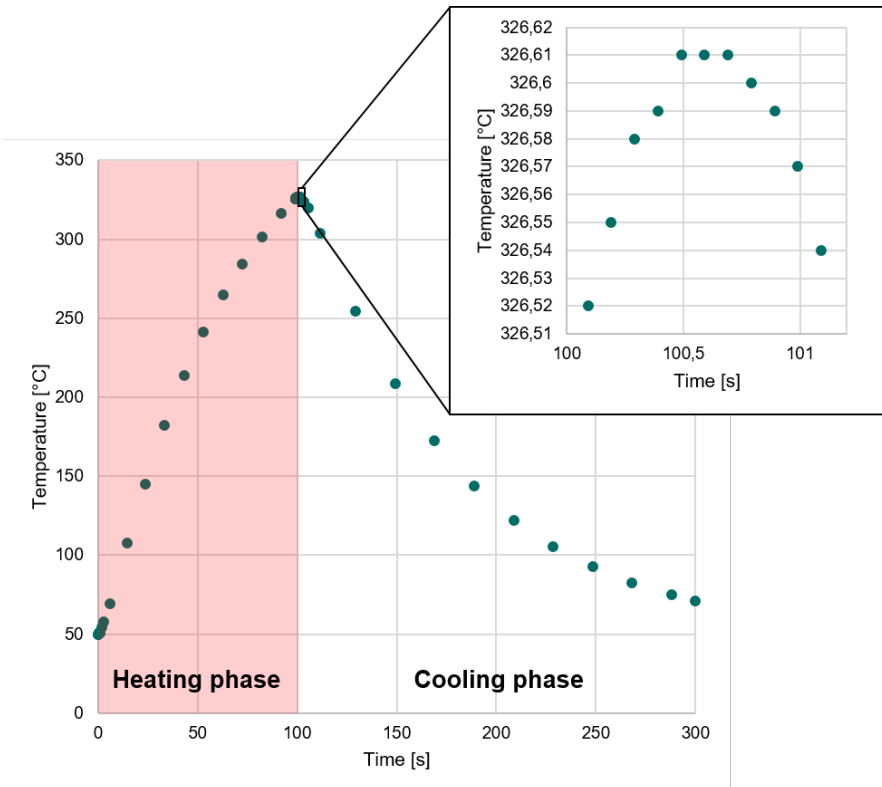


Figure 5.11: *Evolution of the maximum temperature of the CuCrZr heat sink for 100 s pulse and 300 s cooldown.*

The results show that the latent heat diffusion phenomenon is negligible with a temperature increase of approximately 0,1 °C over the span of about 0,5 s. This temperature increase is very small and doesn't greatly affect the general behavior of the tile assembly.

5.3 STATIC STRUCTURAL ANALYSIS

The reflector tile assembly is a highly constrained mechanical system that won't just face high thermal flux but also is mounted on a complex frame. The heat sink is brazed on a tube that runs along the whole module with other heat sinks from other tiles brazed onto it. Some of the tiles are held using support pins welded on the PV. Those pins have a limited range of motion that could potentially negatively impact the structural integrity of the tile. Structural analysis will help understand the local mechanical behavior of the tile as well as the influence of the BCs.

5.3.1 Analysis of the boundary conditions influence

In his 2019 analysis [10], J. Zhu performed his FE analysis using specific BCs which were:

- One end of the SS cooling pipe fixed.
- The other end completely free.

This strategy is a good approach but could be not realistic by allowing too much motion. This is why it is important to test if this modelling strategy influences the results. This BCs set will be used as a reference and a series of simulations will test other BCs with different numbers of degrees of freedom. This should help assess the impact of the tube and the neighbors of the studied tile on its mechanical behavior.

To perform this analysis, first, the model used for the thermal analyses is reused (to stay consistent with the modelling). The boundary conditions are the same as the ones from [10].

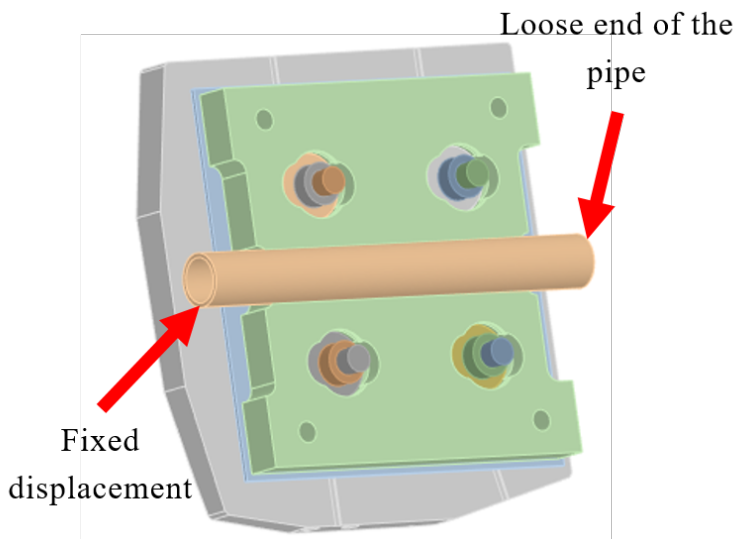


Figure 5.12: Boundary conditions for the reference case (0).

For an accurate modelling of the tube and the heat sinks, the whole module (*H – 02*) 4.3 is cut to only feature the two supports on which the reflector tile heat sink is brazed on. The model doesn't feature the graphite/TZM tiles nor the bolting system to simplify the calculations.

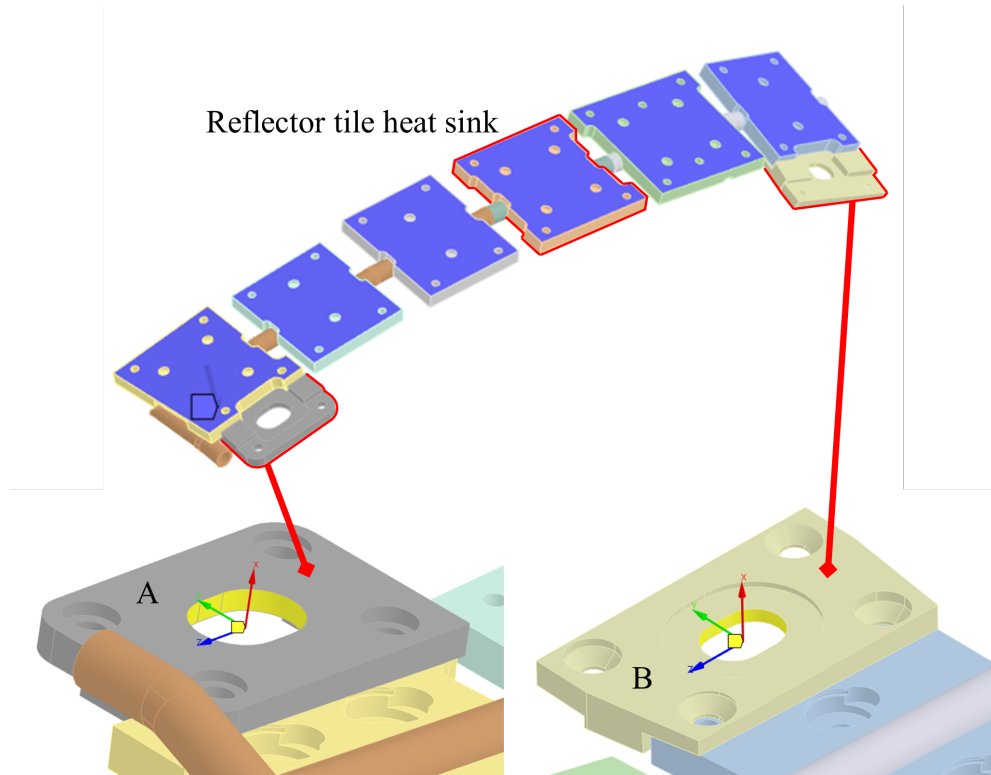


Figure 5.13: View of the third of module *H – 02* with the support parts and heat sinks of adjacent tiles. *A* is the support that will be jointed and *B* is the fixed support

The supports are welded onto the PV but can still move in some directions. The motions of *A* is controlled via a remote displacement (which works like a screw with three translational DoF {TX,TY,TZ} and three rotational DoF {RX,RY,RZ}) whose DoF are piloted by load cases.

<i>Load cases</i>	<i>TX</i>	<i>TY</i>	<i>TZ</i>	<i>RX</i>	<i>RY</i>	<i>RZ</i>
1	0	0	free	0	0	0
2	0	0	free	free	0	free
3	0	0	free	free	free	free
4	0	free	free	free	free	free
5	free	free	free	free	free	free

Table 5.5: Table of free and fixed DoF for the support *A*.

The calculations were done using a coupled-field (thermal and structural) solver for practical reasons, one-way coupling would also have been perfectly adapted to this problem. The results of the analysis show different maximum displacement of the module.

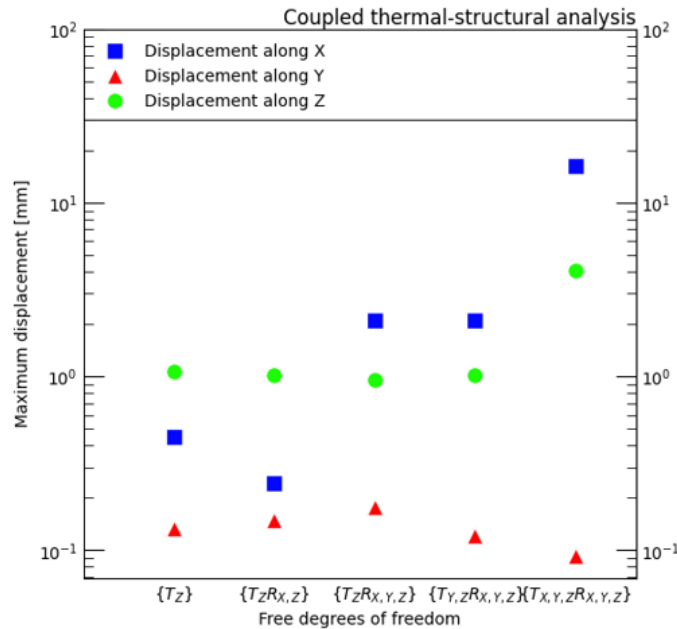


Figure 5.14: Maximum displacement of the module in function of freed *DoF*.

To further assess the validity of the model, it is possible to compare the maximum stress of the model for each load case to the Case 0. The stress shouldn't change with respect to load case and only change because of fictitious stress concentration introduced by the mesh.

Heat sink stress for Case 0	Loadcase	Heat sink max. stress	Relative deviation to case 0
[Pa]	-	[Pa]	%
8,66E+08	1	7,66E+8	11,5
8,66E+08	2	7,65E+8	11,6
8,66E+08	3	7,91E+8	8,6
8,66E+08	4	8,03E+8	7,3
8,66E+08	5	8,85E+8	2,2

Table 5.6: Comparison of the maximum stress concentration in the heat sink.

It is possible to conclude that the boundary conditions of Case 0 are usable as is for further structural calculations.

5.3.2 Contact status after calculations with 100 % contact between TZM-tile and Sigraflex thermal gasket

While performing the structural analysis, the contact status changed. Because the parts of the tile assembly would bend and deform due to thermal expansion, some contacts, namely the **TZM** tile/Sigraflex contact and the Sigraflex/**CuCrZr** heat sink contact would be broken making heat transfer via conduction impossible. The surface area would be smaller and there would not be as much heat evacuated. The 100 % contact model thus doesn't accurately represent reality.

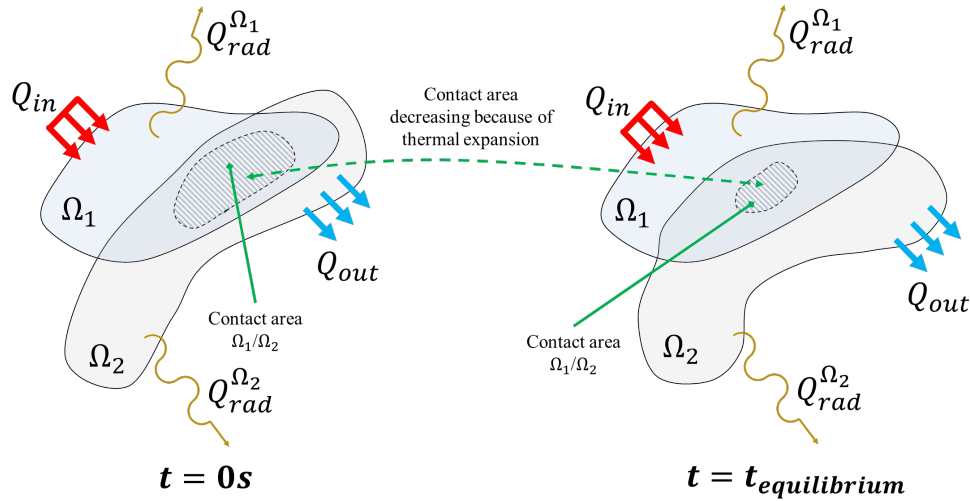


Figure 5.15: Contact area reduction phenomenon.

In steady-state, the input heat load Q_{in} is constant. What happens is the decrease of contact area between the two domain Ω_1 and Ω_2 limiting the heat transfer from Ω_1 to Ω_2 . The evacuated power Q_{out} is thus lower. Because of energy conservation, the heat radiated by Ω_1 is higher, increasing its temperature while the temperature of Ω_2 is lower. This then leads to the first approach to coupled analysis. A first simple method was developed to "manually" update the contact geometry based on the results of the structural analysis.

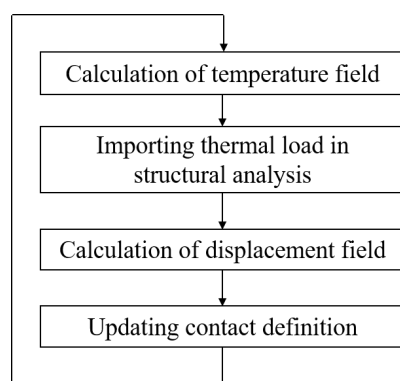


Figure 5.16: Manual coupling method.

It is possible to test this method and perform the **FE** analysis.

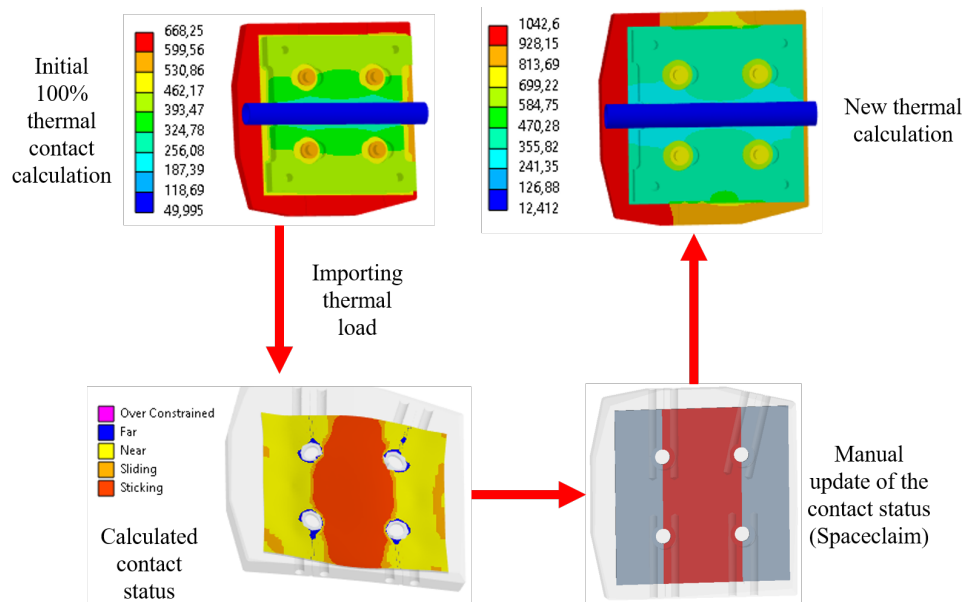


Figure 5.17: Temperature in °C. Application of the manual coupling.

In the figure above 5.3.2, it is possible to see that the temperature field of the TZM reflector tile is higher for the updated contact model. This is in accordance with the prediction by the general model 5.3.2. The issue with the manual update is the inaccuracies subsequently introduced by this manual approximation of the new contact configuration. When static structural analysis is performed on the new model, it is possible to see that the contact area tends to shrink, which is in reality not the case.

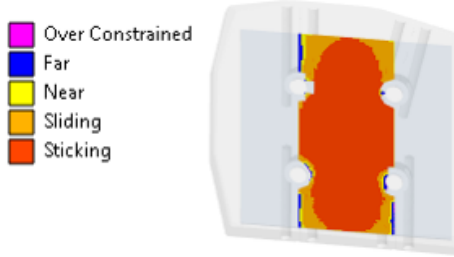


Figure 5.18: Contact shrinking after structural recalculation.

This conclusion leads to the logical choice of carrying out a fully coupled fields analysis to counter this complex coupled problem.

5.4 COUPLED FIELDS ANALYSIS

In the above chapter, it was concluded that complex coupled phenomena such as temperature and displacement dependant contacts. To understand the coupling method and its mathemat-

ical implications, a little introduction to coupling will be done.

5.4.1 Introduction to coupled fields analysis

There are many different methods for multiphysics coupling. This idea of coupling fields is to consider the effect of field A on field B and vice-versa using coupling terms.

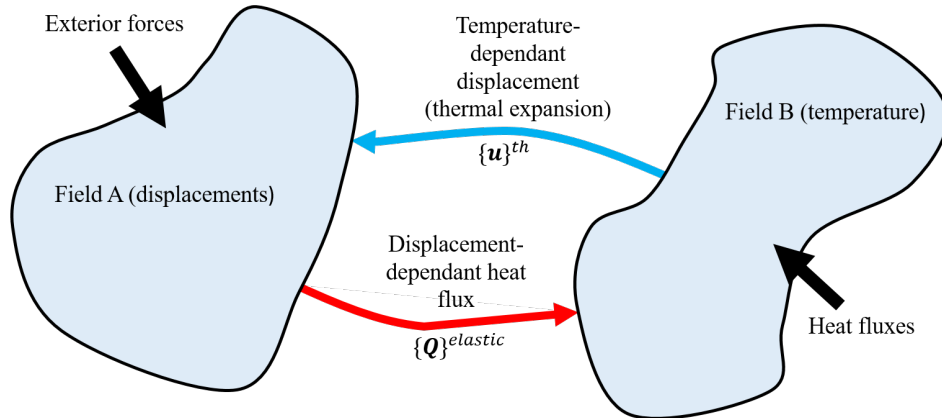


Figure 5.19: Fields coupling.

The coupling can be made of two different levels, the weak coupling (vector coupling) and the strong coupling (matrix coupling). The vector coupling is generally less computationally expensive. It works by adding to the right-hand side of the equation a coupling vector.

$$\begin{bmatrix} K[1,1] & 0 \\ 0 & K[2,2] \end{bmatrix} \left\{ \begin{array}{l} \{\text{Displacement field}\} \\ \{\text{Temperature field}\} \end{array} \right\} = \left\{ \begin{array}{l} \{\text{Forces}\} + \{\text{Forces}\}_{\text{thermal}} \\ \{\text{Heat fluxes}\} + \{\text{Heat fluxes}\}_{\text{th. elastic}} \end{array} \right\} \quad (5.3)$$

This method is less computationally expensive since the coupling is done by adding the coupling vector. The system matrix is diagonal, meaning that it is possible to decouple the calculation of the displacement field and the temperature field and create two subproblems such that:

$$K[1,1]\{\text{Displacement field}\} = \{\text{Forces}\} + \{\text{Forces}\}_{\text{thermal}} \quad (5.4)$$

and the other

$$K[2,2]\{\text{Temperature field}\} = \{\text{Heat fluxes}\} + \{\text{Heat fluxes}\}_{\text{th. elastic}} \quad (5.5)$$

This also means that the fields are NOT calculated at the same time but rather one after the other. The method while taking less storage space requires more steps. Another way to couple the fields is using the strong coupling (matrix coupling). In this method, the fields are no longer coupled using a coupling vector but rather directly in the system matrix by introducing off-diagonal coupling terms $K[1,2]$ and $K[2,1]$. Those terms allow a direct coupling of the fields as well as simultaneous calculations of the solution vector. This method is computationally expensive and will require more storage space but less steps.

$$\begin{bmatrix} K[1,1] & K[1,2] \\ K[2,1] & K[2,2] \end{bmatrix} \left\{ \begin{array}{l} \{\text{Displacement field}\} \\ \{\text{Temperature field}\} \end{array} \right\} = \left\{ \begin{array}{l} \{\text{Forces}\} \\ \{\text{Heat fluxes}\} \end{array} \right\} \quad (5.6)$$

Weak coupling is the method used in this analysis because the model is not complex, the contact surfaces are plane and the bolting system is not modelled. The preload of the bolts is modelled using forces. Those forces were derived from previous structural only analysis (in average the preload force is 750 W). A comparison with strong coupling 5.6 was done to assess the result differences and the results showed little deviation.

5.4.2 Static thermal-structural analysis of the tile assembly

After these considerations, it is possible to proceed with the calculations. The model is tested for four load cases 5.1.

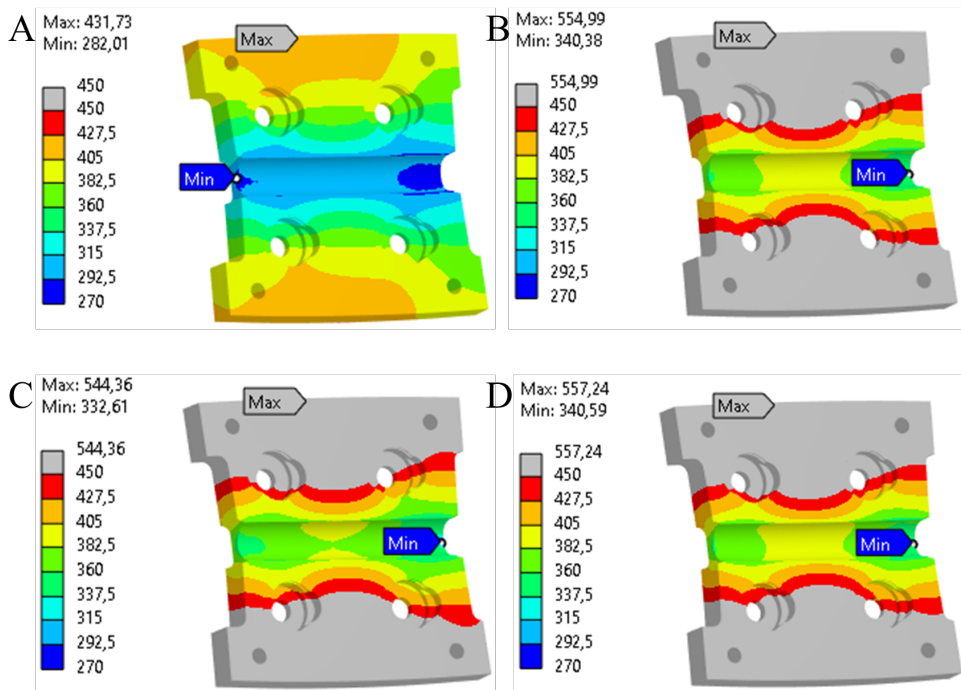


Figure 5.20: Coupled analysis of CuCrZr heat sink per load case. A is plasma heat load only, B is plasma heat load + ECRH axisymmetric heat load, C is plasma heat load + ECRH non-axisymmetric heat load, D is plasma heat load + ECRH axisymmetric heat load (J. Zhu parameters) [10].

The results are showing high CuCrZr temperatures. The maximum temperatures are higher for the coupled analysis compared to the case with 100 % of thermal contact and the manually updated contact. It is possible to compare with a table to get a more direct comparison.

While the coupled analysis can be more handy when it comes to modelling complex phenomena, they are quite complex to set up. The problem of the contact configuration plagued the model by conditionning the problem is such a manner that it becomes unstable and won't properly converge for all DoFs. This is the reason why, for this early multiphysics model, the bolting system had to be excluded.

This table gives insight about the different results, namely, the fact that the coupled

<i>Load cases</i>	<i>Full contact</i>	<i>Reduced contact</i>	<i>Full coupling</i>
Plasma heat load (250 kWm ⁻²)	414,24	406,26	431,73
Plasma heat load + ECRH axisym.	511,67	494,63	554,99
Plasma heat load + ECRH non-axisym.	503,85	487,64	544,36
Plasma heat load + ECRH non-axisym. (J. Zhu param.)	515,88	496,39	557,24

Table 5.7: Temperature table of the **CuCrZr** heat sink per load case vs. modelling method in °C.

analysis will produce much higher maximum temperatures. The results are particularly conservative and better material properties could have predicted different temperatures. For the Plasma heat load + **ECRH** axisymmetric load case the temperature increased by about 10 % (ref. full contact calculations). For the Plasma heat load + **ECRH** non-axisymmetric load-case: temperature increased by about 9,5 % (ref. full contact calculations). When **ECRH** load is applied, large volumes of the heat sink exceed the limit temperature (if max. temperature is 450 °C) (24,8% of the temperature limit for Plasma heat load + **ECRH** axisymmetric load-case and 22,5% of the temperature limit for Plasma heat load + **ECRH** non-axisymmetric loadcase.)

These results show that the optimal way to model the tile assembly and to perform optimal calculations, **it is recommended to used a coupled physics model**. Multiphysics coupling including the bolting system but also including metallurgical phase change could be of use to get information about the state of the different parts during the life cycle of the assembly.

6 | CONCLUSION AND RECOMMENDATIONS

intro to ch6

Bibliography

- [1] Y. Cengel. *Heat Transfer: A Practical Approach*. McGraw-Hill Education, 2004. ISBN: 9780071236447. URL: <https://books.google.de/books?id=xYASMQAACAAJ>.
- [2] Bernd Diekmann and Eberhard Rosenthal. *Energie: Physikalische Grundlagen ihrer Erzeugung, Umwandlung und Nutzung.* de. Wiesbaden: Springer Fachmedien Wiesbaden, 2014. ISBN: 9783658005009 9783658005016. DOI: [10.1007/978-3-658-00501-6](https://doi.org/10.1007/978-3-658-00501-6). URL: <https://link.springer.com/10.1007/978-3-658-00501-6> (visited on 05/08/2024).
- [3] Van Eeten. *Specification of Design Loads for In-vessel Components of W7-X*. Tech. rep. 1-AC-S0005.2. Wendelsteinstraße 1, Greiswald, Germany: Max-Planck Institute for Plasma Physics, Sept. 2022.
- [4] J. Fellinger. *Thermal-mechanical assessment of heat shields and baffles*. Tech. rep. 28Y3JJ. Wendelsteinstraße 1, Greiswald, Germany: Max-Planck Institute for Plasma Physics, May 2013.
- [5] Jeffrey P. Freidberg. *Plasma Physics and Fusion Energy*. Cambridge University Press, 2007.
- [6] J. H. Lienhard V and J. H. Lienhard IV. *A Heat Transfer Textbook*. Version 6.00. Cambridge, MA, Apr. 2024. URL: <https://ahtt.mit.edu>.
- [7] Jochen Linke et al. “Challenges for plasma-facing components in nuclear fusion”. In: *Matter and Radiation at Extremes* 4.5 (Aug. 2019), p. 056201. ISSN: 2468-2047. DOI: [10.1063/1.5090100](https://doi.org/10.1063/1.5090100). eprint: https://pubs.aip.org/aip/mre/article-pdf/doi/10.1063/1.5090100/13886520/056201\1_online.pdf. URL: <https://doi.org/10.1063/1.5090100>.
- [8] Axel Lorenz. *OP2 pulse cycles for thermal design layout of IVC*. Tech. rep. 2A5JSF. Wendelsteinstraße 1, Greiswald, Germany: Max-Planck Institute for Plasma Physics, Oct. 2020.
- [9] UDVARDY MIKLOS D. F. “THE ROLE OF THE FEET IN BEHAVIORAL THERMOREGULATION OF HUMMINGBIRDS”. en. In: *The Cooper Ornithological Society* (1983). URL: <https://sora.unm.edu/sites/default/files/journals/condor/v085n03/p0281-p0285.pdf>.
- [10] Jiawu Zhu. *Parametric thermal and mechanical analysis of ECRH reflecting tile (TZM)*. 2019.